Quantification of Aerosol Transmission through Stress Corrosion Crack-Like Geometries

Spent Fuel and Waste Disposition

Prepared for
US Department of Energy
Spent Fuel and Waste Science and Technology

P. Jones, R. J. M. Pulido, A. Perales, and S. G. Durbin
Sandia National Laboratories

August 19, 2022
Milestone No. M2SF-22SN010207074
SAND2022-#### R

Sandia National Laboratories is a multimission laboratory managed and operated by National Technology & Engineering Solutions of Sandia, LLC, a wholly owned subsidiary of Honeywell International Inc., for the U.S. Department of Energy's National Nuclear Security Administration under contract DE-NA0003525.

Prepared by
Sandia National Laboratories
Albuquerque, New Mexico 87185 and Livermore, California 94550

Sandia National Laboratories is a multimission laboratory managed and operated by National Technology & Engineering Solutions of Sandia, LLC, a wholly owned subsidiary of Honeywell International, Inc., for the U.S. Department of Energy's National Nuclear Security Administration under contract DE-NA0003525.

Sandia National Laboratories

NNSA
National Nuclear Security Administration

ABSTRACT

The formation of a stress corrosion crack (SCC) in the canister wall of a dry cask storage system (DCSS) has been identified as a potential issue for the long-term storage of spent nuclear fuel. The presence of an SCC in a storage system could represent a through-wall flow path from the canister interior to the environment. Modern, vertical DCSSs are of particular interest due to the commercial practice of using more significant backfill pressures in the canister, up to approximately 800 kPa. This pressure differential offers a relatively high driving potential for blowdown of any particulates that might be present in the canister. In this study, the rates of gas flow and aerosol transmission of a spent fuel surrogate through an engineered microchannel with dimensions representative of an SCC were evaluated experimentally using coupled mass flow and aerosol analyzers. The microchannel was formed by mating two gage blocks with a linearly tapering slot orifice nominally 13 µm (0.005 in.) tall on the upstream side and 25 µm (0.0010 in.) tall on the downstream side. The orifice is 12.7 mm (0.500 in.) wide by 8.86 mm (0.349 in.) long (flow length). Surrogate aerosols of cerium oxide, CeO_2, were seeded and mixed with either helium or air inside a pressurized tank. The aerosol characteristics were measured immediately upstream and downstream of the simulated SCC at elevated and ambient pressures, respectively. These data sets are intended to add to previous testing that characterized SCCs under well-controlled boundary conditions through the inclusion of testing improvements that establish initial conditions in a more consistent way. These ongoing testing efforts are focused on understanding the evolution in both size and quantity of a hypothetical release of aerosolized spent fuel particles from failed fuel to the canister interior and ultimately through an SCC.

This page is intentionally left blank.

ACKNOWLEDGEMENTS

This work was funded by the U.S. Department of Energy (DOE), Office of Nuclear Energy Spent Fuel and Waste Disposition Research and Development Program.

The authors would like to express their appreciation to Ned Larson of the DOE for his programmatic leadership and vision. The technologist team of Greg Koenig, Thad Vice, Ron Williams, and Beau Baigas are commended for their tireless efforts and attention to detail in making this work possible.

This page is intentionally left blank.

CONTENTS

LIST OF FIGURES

LIST OF TABLES

This page is intentionally left blank.

ACRONYMS

AED	aerodynamic equivalent diameter
alpm	actual liters per minute
DCSS	dry cask storage system
DOE	US Department of Energy
EDM	electrical discharge machining
FS	full scale
GSD	geometric standard deviation
HEPA	high-efficiency particulate absorbing
MMD	mass median diameter
NE	Nuclear Energy
ORNL	Oak Ridge National Laboratory
PNNL	Pacific Northwest National Laboratory
PWR	pressurized water reactor
RBG	rotating brush generator
SCC	stress corrosion crack
SFWD	Spent Fuel and Waste Disposition
slpm	standard liters per minute
SNF	spent nuclear fuel
SNL	Sandia National Laboratories
STP	standard temperature and pressure

This page is intentionally left blank.

QUANTIFICATION OF AEROSOL TRANSMISSION THROUGH STRESS CORROSION CRACK-LIKE GEOMETRIES

This report fulfills milestone M2SF-22SN010207074 in the Aerosol Source Term work package (SF-22SN01020707). This work was sponsored under the Department of Energy's (DOE) Office of Nuclear Energy (NE) Spent Fuel and Waste Disposition (SFWD) campaign.

1 INTRODUCTION

Dry cask storage systems (DCSSs) for spent nuclear fuel (SNF) are designed to provide a confinement barrier that prevents the release of radioactive material, maintains SNF in an inert environment, provides radiation shielding, and maintains subcriticality conditions. SNF is initially stored in pools of water for cooling where the water also provides radiation shielding. As these pools get closer to capacity, dry storage systems are becoming the primary means of extended storage. After sufficient cooling in pools, SNF is loaded into a canister and placed inside a storage cask, where the canister is welded shut. The DCSS is then decontaminated and dried, and the system is moved to an on-site dry storage location. Figure 1.1 shows the major components of a DCSS for SNF.

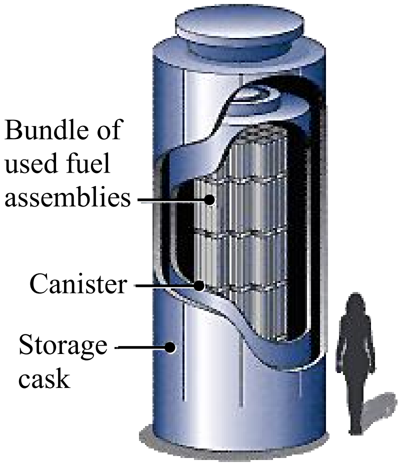

Source: https://www.nrc.gov/waste/spent-fuel-storage/diagram-typical-dry-cask-system.html

Figure 1.1 Typical dry cask storage system.

Typically, the canisters are made of stainless steel. The dry storage system is designed with an open volume between the canister and the storage cask. Rejection of the decay heat is accomplished by air flowing from air inlets at the bottom of the cask to outlets at the top via natural convection. This passively cooled design also allows dust from the environment into the system. These particulates may then collect on the surfaces of the canister. As the SNF cools, salts contained in the dust may deliquesce in the presence of moisture from the ambient relative humidity to form concentrated brines, which may contain corrosive species such as chlorides. These species can cause localized corrosion, called pitting. With sufficient stresses, these pits can evolve into stress corrosion cracks (SCCs), which could penetrate through the canister wall and allow communication from the interior of the canister to the external environment [Schindelholz, 2017].

1.1 Objective

The purpose of this on-going research is to explore the characterization of aerosols in DCSSs that have developed a through-wall SCC. The characteristics of interest include particulate suspension, transport, depletion, and transfer/deposition in the SCC.

This testing employed engineered slots with characteristic dimensions similar to those in SCCs as analogs. A more advanced geometry was explored in FY21 and iterated with more scrutiny in this testing to better approximate SCCs.

A Palas Promo 3000 HP high resolution aerosol spectrometer has been integrated into the experimental system that can directly monitor aerosol samples at elevated pressures. This high-pressure aerosol characterization system is designed to opto-mechanically switch between monitoring upstream and downstream sensing detector elements offering nearly simultaneous real-time measurements and eliminating the instrument bias seen in previous testing [Durbin *et al.*, 2018]. This test apparatus has consistently demonstrated a flexible technological approach to directly measure aerosol transmission through the engineered microchannel/slot at conditions of interest.

1.2 Previous Studies

The data obtainable from the measurement of particulate segregation in flows through open channels has significance in multiple fields. Studies include particle penetration through building cracks [Lewis, 1995, Liu and Nazaroff, 2003, Mosley *et al.*, 2001] to nuclear reactor safety [Powers, 2009], and more recently, storage and transportation of SNF in dry casks [Durbin *et al.*, 2020 & 2021]. Studies of these systems contribute to the understanding of particulate segregation through small channels as functions of particle size and concentration, channel dimensions, and differential pressures.

Previous work has contributed to the characterization of particulate segregation across channel flow for a range of particle sizes in aerosols. Lewis [Lewis, 1995] was motivated by a lack of empirical studies to support the development of protection factors against solid particles for enclosures. This protection factor was taken as the ratio of the dose of an outside concentration of particulates to the dose accumulated inside an enclosure for a specified time, with the doses defined as concentration-time integrals. Models were derived describing the total transport fraction of particles across a rectangular slot into an enclosure as functions of particle size, differential pressures, and slot heights. Lewis described an experimental apparatus with synthesized aerosols (containing either talc, aluminum oxide, titanium oxide, various silica powders, or ambient dust) mixed in a chamber containing an enclosure with a rectangular slot open to the chamber. A differential pressure was established between the chamber and the enclosure. Protection factors were found by comparing mass concentration values inside and outside the enclosure over a given time. The primary observations here were the decrease in total transport fraction with increasing particle size from 1-10 µm as well as a decrease in protection factor (corresponding to an increase in total transport fraction) with increasing differential pressures and slot heights.

Liu and Nazaroff [Liu and Nazaroff, 2003] conducted experiments of aerosol flow through rectangular slots using various building materials, including aluminum, brick, concrete, and wood. The slot heights were 0.25 mm and 1 mm, which are large compared to the micron- to submicron-sized particles they flowed through the cracks. They obtained data for particle penetration (defined as the ratio of downstream to upstream particle concentration), related to total transport fraction, as a function of particle size. They found that, for 0.25 mm cracks, particle sizes between 0.1-1 µm achieved penetration factors near unity, while smaller and larger particles showed diminished penetration factors for pressure differentials of 4 and 10 Pa. Meanwhile, for 1 mm slot heights, the penetration factors were near unity for the majority of the particle size distribution. Their results matched closely with models they created from analysis of particle penetration through simplified cracks [Liu and Nazaroff, 2001] and had similar qualitative conclusions to Lewis's work.

Mosley studied particle penetration through a 0.508 mm slot height between aluminum plates with particles of aerodynamic equivalent diameters (AEDs) from 0.1 to 5 µm [Mosley *et al.*, 2001]. They found penetration factors close to unity for particle sizes between 0.1-1 µm, with a sharp drop-off in penetration factor for particle sizes larger than 1 µm for pressure differentials between 2 and 20 Pa – this was consistent with Liu and Nazaroff's results when considering the order of magnitude of the pressure differentials and particle size distributions.

The motivation behind the above work was based on ambient particle penetration of enclosures and the number of particles subject to human exposure, with slot heights and pressure differentials corresponding to conditions typically associated with building cracks and pressure differences between indoor and outdoor environments, respectively.

Casella studied the flow from pinhole breaches and particle deposition inside the breach for canisters with moderate pressure backfills [Casella *et al.*, 2006, Casella *et al.*, 2007]. The pinholes examined in these studies were relatively small, with diameters on the order of 10 µm. The particulates considered were also relatively small, with diameters of 0.05 to 0.1 µm. The initial, internal canister backfill pressure was 188 kPa. These analytic studies demonstrated that the effect of channel plugging can greatly reduce the leak rate from a canister.

However, the channel dimensions considered do not apply to the channel geometry associated with SCCs from potential corrosion of dry casks. The literature reports typical crack heights to be around 16 to 30 µm [EPRI, 2014 & 2017; Meyer *et al.*, 2016] and internal pressures of 100 to 760 kPa (14.5 to 110 psig) [EPRI, 2017] for a range of cask models. Therefore, an apparatus and procedures were developed to investigate a slot height on the order of 10 µm and pressure differentials on the order of 100 kPa to supplement the established database of particulate transmission in microchannel flows. This experimental approach has demonstrated adaptability for future testing of more prototypic stress corrosion crack geometries. Preliminary results using air as the carrier gas indicated 44% of the aerosols available for transmission were retained upstream of the microchannel [Durbin *et al.*, 2018].

1.3 Current Study and Collaborative Modeling

1.3.1 Uniqueness of Current Study

An aerosol spectrometer is utilized for this study to measure the size resolved aerosol concentration, also known as aerosol size distribution. The Palas Promo 3000 HP is fiber-optically coupled to two Welas 2200 high pressure aerosol sensors. The high-pressure aerosol sensor directly samples gas streams at native pressures up to 1.0 MPa. Rapid fiber optic switching allows a single instrument to analyze the upstream and downstream aerosol sensors in quasi-simultaneous fashion using the same optical detector. Switching of upstream and downstream sensors occurred every 60 seconds (see Section 2.3.4 for details). Thus, instrument bias was eliminated, and sample line losses were substantially minimized.

This study is a continuation from previous microchannel aerosol transport testing at Sandia National Laboratories (SNL) [Durbin et al., 2021] using a microchannel with a depth that varies linearly from 13 to 25 µm (more details in Section 2.2). This testing differs from the uniform 28.9 µm simple slot orifice tested previously (SNL) [Durbin et al., 2020] and is more representative of the microchannel profile that results from the evolution of a stress corrosion crack. This choice of geometry is the next step following testing of a simple slot orifice. The subsequent step will involve testing of lab grown SCCs; however, because the lab grown cracks will be limited to a single use, additional testing of the diverging micro-channel was conducted to further refine the calibration and testing procedures. The results of the refinements explored in FY22 are presented here.

The aerosol transmission through the linearly varying microchannel orifice was measured from tests using either air or helium as the fill gas at similar pressure differences between the upstream and downstream test sections. The procedure in which aerosols were introduced was kept as consistent as practical across tests for both fill gases. However, there were some procedural differences in the testing at the various pressure levels of interest when using helium versus air. Through this methodology, comparisons in aerosol transmission between two distinct pressurized gas environments were made.

1.3.2 Collaborative Modeling Efforts

Modeling efforts from Pacific Northwest National Laboratory (PNNL) and Oak Ridge National Laboratory (ORNL) in collaboration with Purdue University are being conducted in parallel to the modeling and experimental efforts from SNL. The focus of these efforts can be localized to two separate areas as illustrated in Figure 1.2.

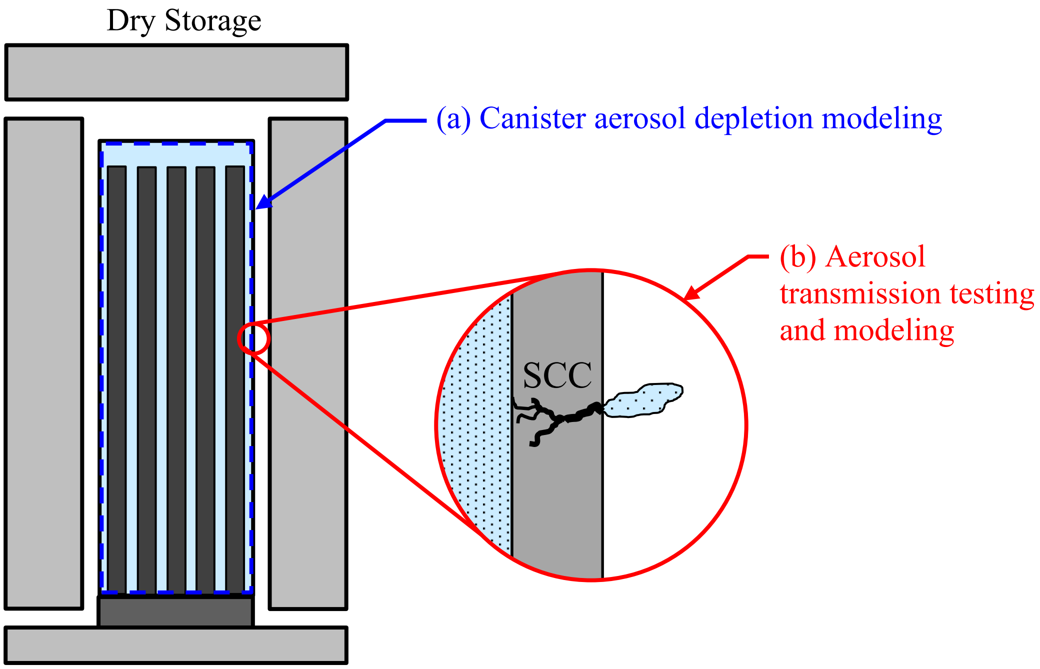

Figure 1.2 Collaborative modeling and testing areas.

GOTHIC modeling at PNNL [Lanza *et al*., 2021, Lanza *et al*., 2022] and MELCOR modeling by Phillips and Gelbard at SNL [Phillips and Gelbard, 2021, Phillips, 2022] focus on aerosol deposition within the canister internal volume (Figure 1.2(*a*)). First principles modeling of aerosol transport/depletion in microchannels by Chatzidakis at Purdue University and Sasikumar at ORNL [Chatzidakis and Sasikumar, 2021] as well as the experimental study presented in this report focus separately on aerosol transmission through a stress corrosion crack (Figure 1.2(*b*)). The modeling and experimental efforts running in parallel across multiple national laboratories will serve to develop further understanding of aerosol transport phenomena in DCSSs and SCCs.

2 APPARATUS AND PROCEDURES

The experimental approach adopted for these studies is similar to previous studies [Lewis, 1995; Mosley *et al.*, 2001; Liu and Nazaroff, 2001 and 2003] in that aerosol analyzers are used to characterize the particle size distribution and concentration present in the gas before and after flowing through a simulated crack. Because these previous studies considered aerosol transport through building walls or containment structures, the focus was on flows through relatively wide and long slots driven by constant low pressure drops. In the present study, consideration was given to aerosol transport through dry storage canister walls. Here, the focus was on much narrower and shorter microchannels that represent stress corrosion cracks through the canister wall with aerosol transport driven by initially higher pressure drops across the wall.

Two types of tests were considered for these studies. In the first test type, denoted as a “blowdown,” the storage tank was pressurized, isolated from the pressure source, and allowed to blowdown to ambient pressure via the microchannel. In the second test type denoted as “constant pressure,” the pressure in the storage tank was maintained at a constant value with a pressure controller as flow is directed through the microchannel. The blowdown type of test more closely simulated the expected behavior of a pressurized SNF canister. While not prototypic, the constant pressure tests decoupled the pressure transient, which allowed better examination of the SCC discharge characteristics as it was fouled with deposited particulates. The majority of testing in FY22 was at constant pressure. Testing was conducted with both dry air and helium as the aerosol carrier gas. DPCs are backfilled with helium, and in the event a SCC were to develop, the backfilled helium would vent through the SCC to atmosphere. As such, helium is the natural and preferred choice of aerosol carrier gas. From an operational perspective, the use of dry air as the carrier gas is enticing due to its abundancy and affordability.

2.1 General Construction and Operation

The general layout of the experimental setup is illustrated in Figure 2.1**Error! Reference source not found.** and Figure 2.2**Error! Reference source not found.**. A 0.908 m^3 (240 gal) pressure tank is used to simulate the canister. Several stirring fans were installed roughly along the tank centerline to stir the particulates and minimize aerosol depletion through deposition of particles on the inner surface of the tank over the course of a test. The tank was initially loaded with a measured quantity of dry powder aerosols using a Palas rotating brush generator (RBG). See Section 0 for more details on the RBG. The desired and actual initial aerosol concentrations are discussed in Section 2.4.2.

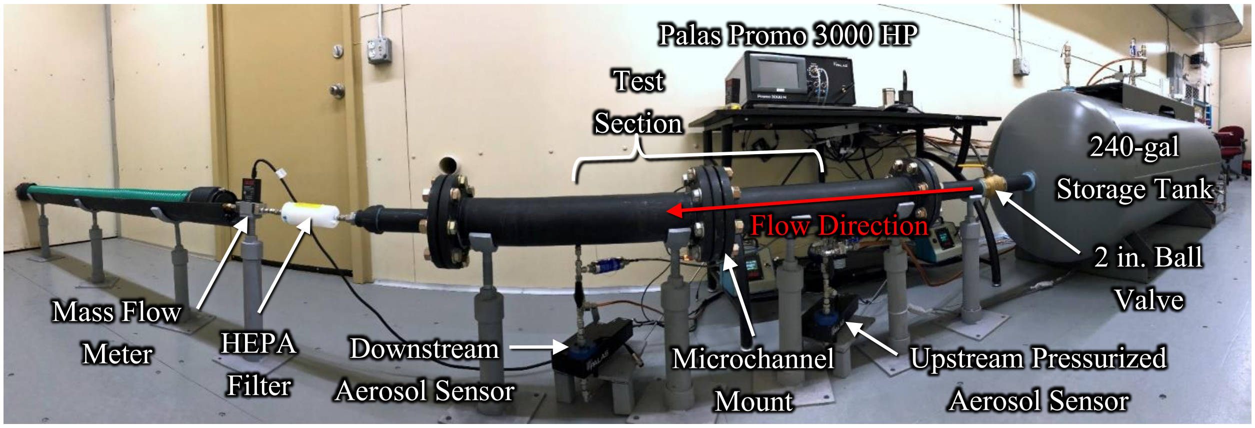

Figure 2.1 General layout of the experimental apparatus.

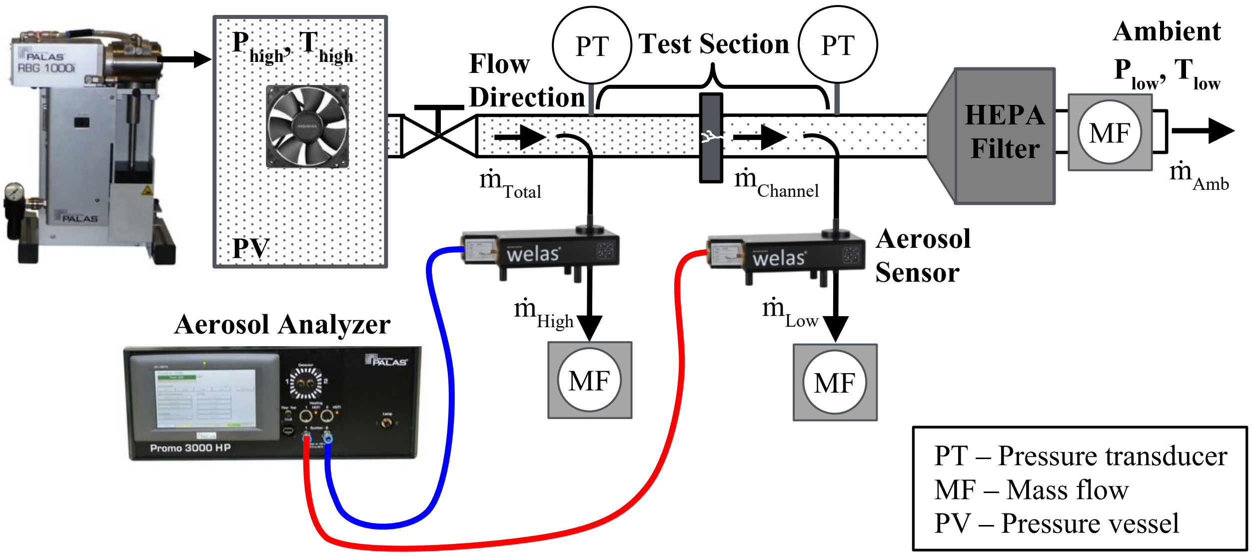

Figure 2.2 **Schematic of the experimental apparatus showing the major components.**

Clean air or helium was used to displace ambient air out of the upstream and downstream portions of the test section. The pressure tank was pressurized up to operating pressure. A Palas Promo 3000 HP spectrometer and Welas 2200 high pressure aerosol sensor were used to monitor aerosol concentration in the pressure tank up to concentrations of 1.6×10^4 particles/cm^3. If the aerosol concentration was higher than desired, the tank was briefly purged through a valve venting to atmosphere and re-pressurized as needed until the target mass concentration was achieved. The duration of time between initial seeding and test initiation was reduced as much as feasible to limit the settling of the larger, heavier particles. A pressure controller maintained and supplied clean air (or helium) to the pressure tank for the duration of the constant pressure tests; for blowdown tests, the clean air (or helium) supply to the pressure tank was turned off just before test initiation.

Tests are initiated by opening the 2-inch ball valve which releases the particle laden flow into the test section. Gas flow exhausts to ambient either through the mass flow meter at the end of the test section, or through the aerosol sensors and associated mass flow controllers. The engineered microchannel, containing an SCC-like geometry, was mounted in the middle of the test section comprised of mounting flanges and two 0.61 m (24 in.) long, 0.10 m (4 in.) diameter schedule 40 pipe nipples (see Figure 2.2). A sample stream was drawn from the centerline at the nipple midpoint (0.30 m from the microchannel) on the high-pressure upstream and low-pressure downstream sides of the test microchannel. Smooth bend 90° fittings are installed inside the pipe nipples with the inlet facing the flow and serves as the sample line for the aerosol sensors.

Aerosol size and concentration is characterized using identical Welas 2200 high pressure aerosol sensors monitored by a single Palas Promo 3000 HP analyzer. Operational improvements with respect to the Promo 3000 calibration procedures were explored in FY22 which led to changes compared to FY21 (see Section 2.3.4). Flow controllers meter the sample flow through each of the aerosol sensors at a constant rate of 0.5 alpm. In cases where the flow required for the downstream Welas sensor was greater than the flow through the crack, a cover gas was used so that ambient air was not drawn from the exhaust portion of the test section through the sensor. Gas flow from the tank and through the test section was measured by a mass flow meter downstream of the test section. Pressure transducers monitor the upstream and downstream sides of the microchannel, the tank, and ambient pressures. Thermocouples are also installed at the same locations. A low pressure drop, high-efficiency particulate absorbing (HEPA) filter was used to remove all aerosols from the exhaust stream before the final mass flow measurement.

2.2 Design of the Microchannel

The microchannel used in this study has a slot opening that gradually increases in a linear fashion from 13 µm to 25 µm, with the 13 µm depth facing the upstream portion of the test section as illustrated in Figure 2.3. The microchannel was fabricated from paired high-precision Mitutoyo gage blocks as shown in a schematic in Figure 2.4. The microchannel was formed by machining into the surface of one of the gage blocks using electrical discharge machining (EDM). The mounting holes were also cut using wire EDM. The paired halves of the gage blocks were bolted together to form the microchannel held in a mounting assembly as detailed in Figure 2.5. An isometric view of the microchannel mounted to the flow flange is shown in Figure 2.6.

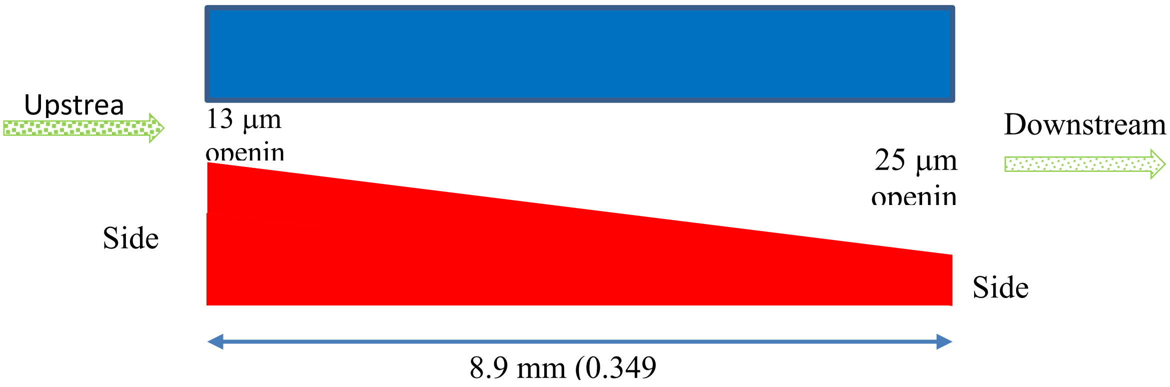

Figure 2.3 Illustration of the linear slot microchannel (not to scale).

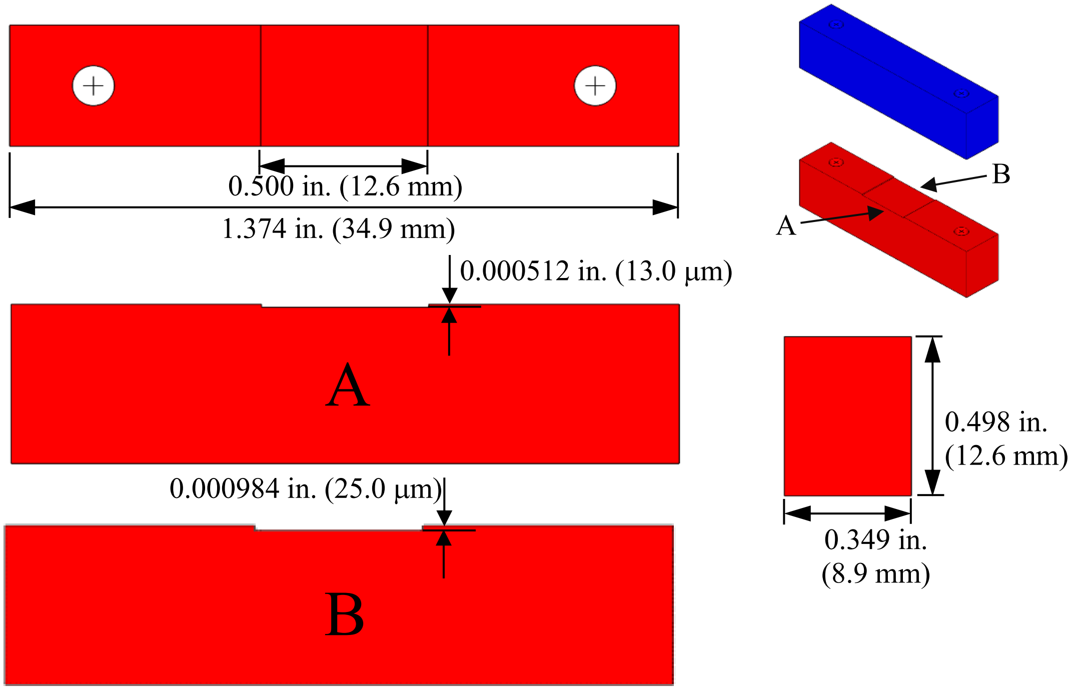

Figure 2.4 Schematic of the linear block (13 to 25 µm depth transition) microchannel assembly. Side A (13 µm depth) faces towards the upstream portion of the test section. Side B (25 µm depth) faces towards the downstream portion.

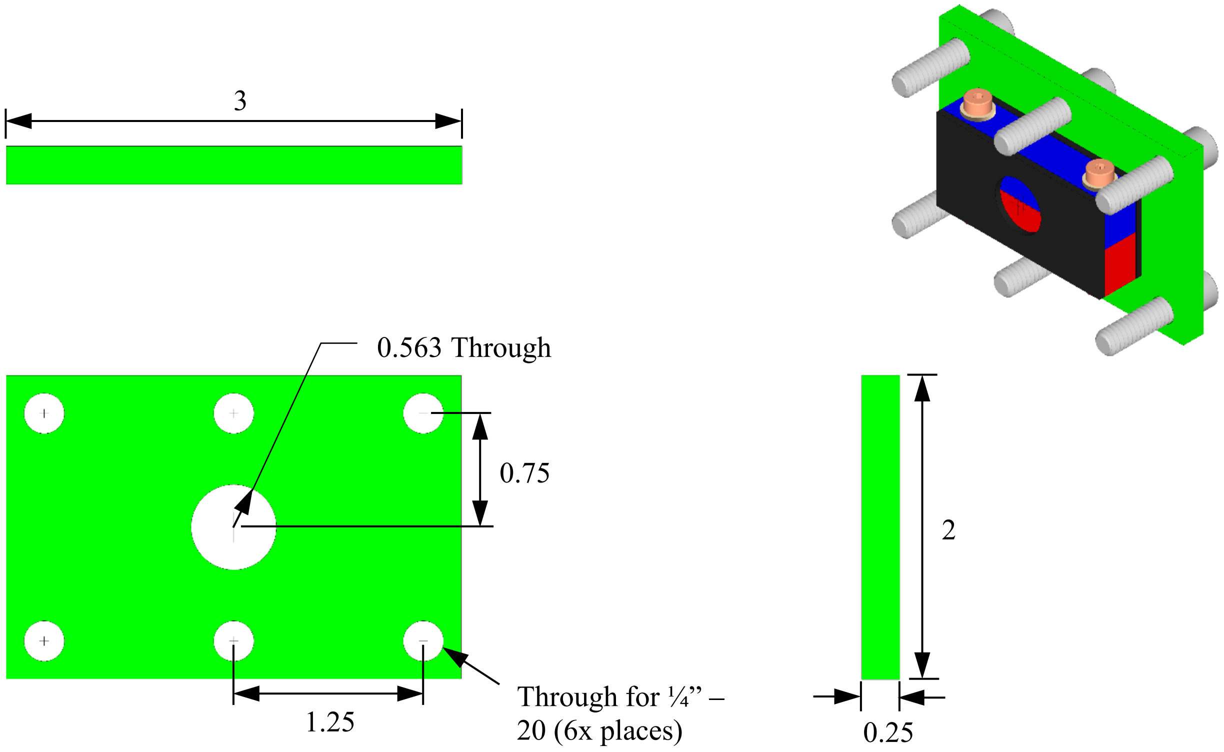

Figure 2.5 Details of the microchannel mounting assembly. All dimensions in inches.

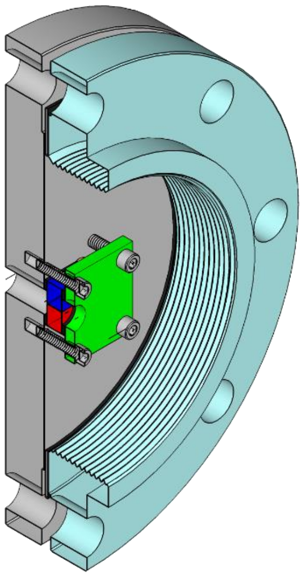

Figure 2.6 Isometric cutaway showing the microchannel mounted to the flow flange.

Figure 2.7(*a)* and Figure 2.7(*b)* show a profilometry image and a corresponding line scan of the linear microchannel block, respectively. These profiles were taken with a Keyence VK-X100 laser scanning microscope.

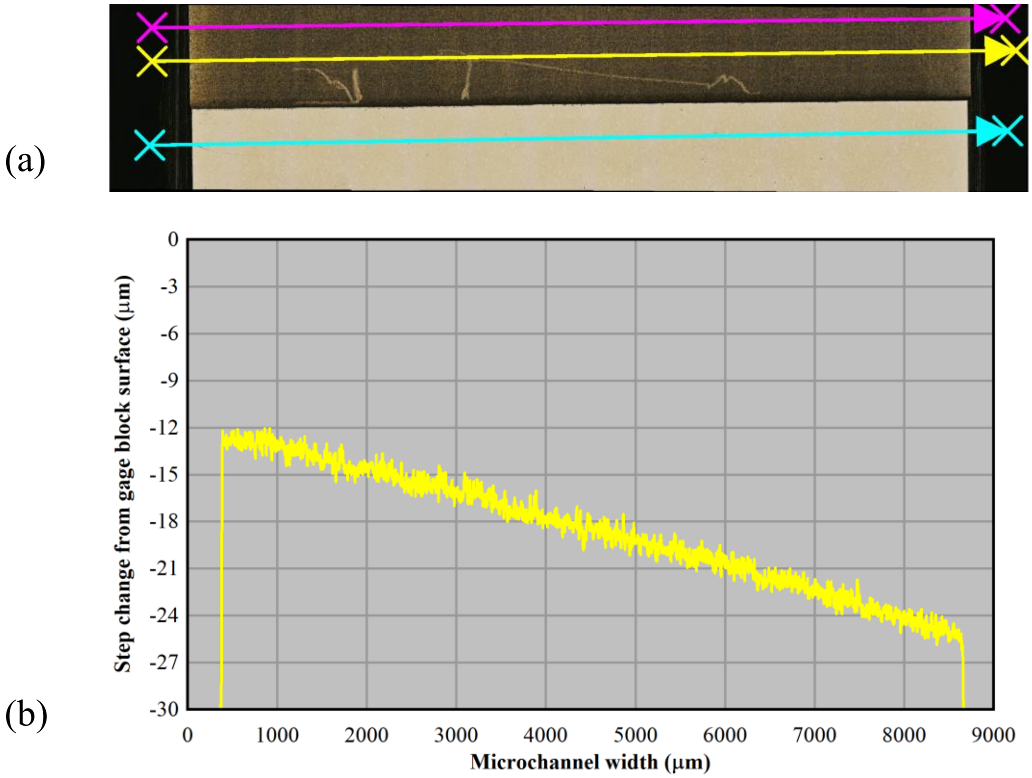

Figure 2.7 Profilometry image (a) and line scan of the linear block (13 to 25 µm depth transition) microchannel (b) using the Keyence laser scanning microscope.

The drop-offs in Figure 2.7(*b*) can be explained by the geometry of the microchannel block, which has chamfers along the edges of the block. Figure 2.8 shows these chamfers in more detail. The linear slope region spans 8.26 mm across the microchannel width, but the total width of the block is 8.89 mm, so 0.63 mm of the flow length is chamfered.

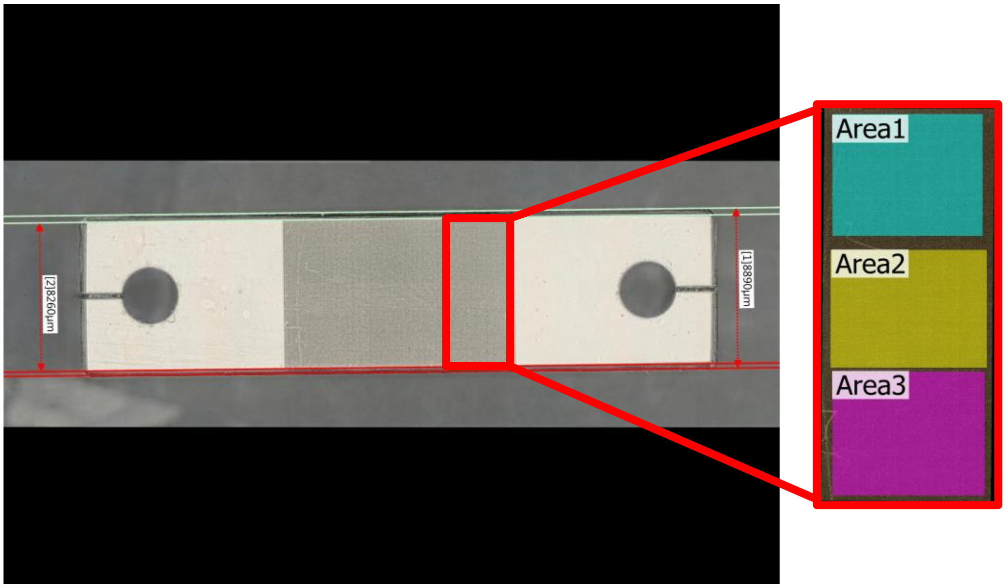

Figure 2.8 Optical microscope image of the linear block detailing the chamfered regions, and the region used to characterize the surface roughness

The surface roughness of the microchannel was also characterized with the Keyence VK-X100 laser scanning microscope by taking the arithmetical mean height (S_a) of three surface areas in a sub-region of the microchannel shown in Figure 2.8. The average S_a of the three areas was found to be 0.734 µm, which was on the same order of magnitude as the measured S_a values of the slot orifice microchannel used in previous testing (0.408 and 0.386 µm for the left and right sides of the microchannel region, respectively) [Durbin *et al.*, 2020].

2.3 Instrumentation

The following instrumentation was used to characterize these tests. All stated uncertainties are assumed to represent 95% confidence intervals unless otherwise stated.

2.3.1 Pressure

The pressure in the aerosol storage tank was monitored with a 1,034 kPa (150.0 psia) Setra Model ASM transducer. Pressures on the upstream and downstream sides of the test section were monitored using a 1,034 kPa (150.0 psia) and a 103 kPa (15.0 psia) Setra Model ASM transducer, respectively.

The uncertainty of all the Setra pressure transducers is < ± 0.05% full scale (FS).

Table 2.1 Summary of pressure transducers.

Location	Model No.	Full Scale (kPa)	Uncertainty (kPa)
Storage tank	ASM1-150P-A-1M-2C-03-A-01	2,068	1.03
Upstream	ASM1-150P-A-1M-2C-03-A-01	1,034	0.52
Downstream	ASM1-015P-A-1M-2C-03-A-01	103	0.05

2.3.2 Temperature

All temperature measurements were taken with K-type thermocouples with standard calibration. The suggested, combined uncertainty in these measurements including data acquisition, cabling, and positioning errors is 1% of the reading in Kelvin [Nakos, 2004].

2.3.3 Mass Flow Rate

Flow from the test section was measured by a low pressure drop mass flow meter (Alicat, MW-20SLPM for ΔP ≈ 420 kPa and 720 kPa; MW-2SLPM for ΔP ≈ 120 kPa). The standard liter per minute (slpm) is defined as one liter of air flow at STP (*i.e.,* reference density of $\rho_{STP} = 1.184$ kg/m^3). The mass flow meters used during testing are presented in Table 2.2 and were chosen based on the best match between the starting mass flow rate of each test and the full scale of the mass flow meter. All Alicat flow meters and controllers used are configurable for different gasses, and the presets for air or helium were selected depending on test.

For all the mass flow meters and controllers, the reported 95% uncertainty is ± (0.4% of reading + 0.2% FS) for a maximum of ± 0.6% FS.

Table 2.2 Summary of mass flow instrumentation.

Description	Model No.	Full Scale Q_{STP} (slpm)	Uncertainty (slpm)
High flow downstream exhaust	MW-20SLPM	20	0.12
Mid flow downstream exhaust	MW-10SLPM	10	0.060
Low flow downstream exhaust	MW-2SLPM	2	0.012
High pressure aerosol sensor	MC-5SLPM	5	0.030
Low pressure aerosol sensor	MC-5SLPM	5	0.030

2.3.4 Aerosol Spectrometer and Aerosol Sensors

The Palas Promo 3000 HP is a flexible, light-scattering aerosol spectrometer system that uses twin optical sensors to determine quasi-simultaneous particle concentration and particle size at two locations. Fiber-optic cables (light wave conductor or LWC) are used to carry light from the main controller to the remote Welas 2200 high pressure aerosol sensors as well as the resulting light-scattering signal from the remote sensors back to the main controller. The Welas 2200 sensors are specially designed to require only 0.5 actual liters per minute (alpm) of flow through the sampling chamber. This high-pressure aerosol sensor is capable of directly measuring samples at pressures up to 1,000 kPa. Rapid fiber optic switching allows a single instrument to analyze the upstream and downstream aerosol sensors in quasi-simultaneous fashion.

The instrument collected data from the upstream sensor for 50 seconds in ten-second increments, generating five upstream data points (each consisting of a 10 second average concentration and corresponding 64-channel number count distribution). The switch to the downstream sensor required ten seconds, and then the instrument collected data from the downstream sensor generating another five downstream data points. The nature of the data stream is therefore a series of five data points at 10 second intervals followed by a 60 second gap in data while the other sensor was analyzed.

The aerosol spectrometer characteristics are summarized in Table 2.3. The spectrometer can measure concentrations up to 10^6 particles/cm^3 depending upon the model of the Welas sensor. The spectrometer is ideally suited to simultaneously monitor the aerosols from the high-pressure upstream and low-pressure downstream side of the simulated crack for aerosol size and concentration characteristics. The Welas 2200 can make reliable measurements over a concentration range from 1 to 1.6×10^4 particles/cm^3. The Promo spectrometer will still analyze concentrations in excess of the Welas sensor limit, but it will introduce coincidence error defined as an undercounting of the number of particles and an over estimate of the particle diameter particles because too many particles occupy the measurement volume simultaneously.

In FY22, there was a change in the calibration procedure due to the apparent pressure dependence of particle velocity through the sensor. Calibration of the Promo is conducted using a monodisperse aerosol of known particle diameter. During calibration, the Promo determines the length of the light-scattered signal (pulse width) which is the time of flight (converted to velocity) of a particle through the measurement volume. The user then inputs the measured particle velocity, and the Promo uses the user specified value to correctly map the signal to the appropriate spectrometer channel. Actual particle velocity that deviates from the user specified velocity value will introduce error into the reported concentration and cause the Promo to mis-categorize particles into the wrong size bin.

It was previously thought that the use of flow controllers to maintain sample flow at a constant volumetric flow rate of 0.5 alpm would ensure that the flow velocity through the detection volume remained constant over all operating pressures. This was not the case and the discrepancy was due to the customized "low-flow" Welas sensors. The standard Welas sensor configuration operates at a volumetric flow rate of 5.0 alpm, which was not suitable for this testing. Regardless of sensor configuration, the Promo requires a consistent particle velocity, i.e. time of flight, through the detection volume. In order to maintain consistent particle time of flight for the 0.5 alpm configuration, Palas uses a flow restriction nozzle to accelerate the particles through the detection volume. It is understood that this nozzle introduces the pressure and carrier gas dependence.

To account for pressure dependence, an additional calibration step was introduced in FY22. Calibration prior to the test with the monodisperse aerosol remains unchanged. Once the tank is seeded and at operating pressure, the two-inch ball valve is briefly opened to allow some particles into the upstream test section. The Promo measures the cerium oxide (CeO_2) particle velocity, and that value is input as the new user specified velocity. The impact of this additional calibration on test results is discussed in Section 3.2.5.

Table 2.3 Summary of the aerosol spectrometer capabilities.

Instrument Characteristic	Value
Aerosol size range	0.3 to 17 μm
Aerosol size channels	64/decade
Minimum Particle Concentration	1 particle/cm^3
Maximum Particle Concentration	1.6×10^4 particles/cm^3
Maximum Sample Pressure	1,000 kPa
Maximum Sample Temperature	120 °C

2.3.5 Aerosol Generator

The aerosols were loaded into the pressure tank with a Palas RBG 1000 (Figure 2.9(*a*)) to initialize the test using the desired background gas at a differential pressure of up to 200 kPa. The RBG 1000 can deliver particles at a rate between 40 mg/h to 430 g/h. The heart of the instrument is the rotating brush (Figure 2.9(*b*)). The desired aerosols to be dispersed are packed into a cylinder. A transport piston slowly pushes the bed of packed powder into the rotating metal bristle brush that dislodges particles and holds them in the bristles. When the brush rotates 180 degrees further, the bristles are exposed to a flow of dispersion carrier gas that suspends the particles and transports them away, creating a polydisperse distribution of desired aerosol. The RBG has a maximum operating pressure of 200 kPa which is lower than the maximum testing operating pressure. For the higher pressure tests, the tank had to be seeded at lower pressure, then brought up to operating pressure. This made it difficult to ensure that the target mass concentration was achieved and often required additional steps. If the mass concentration was greater than desired, the tank would be briefly purged and re-pressurized as needed. If less than desired, the tank pressure would have to be reduced to under 200 kPa for the seeding of additional particles.

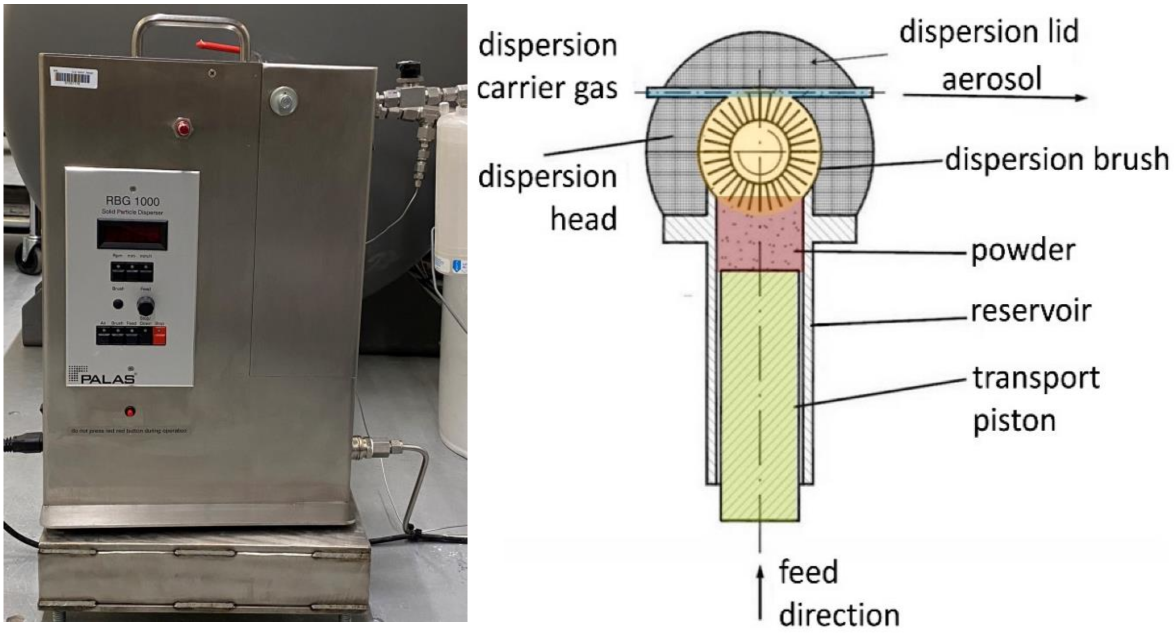

(*a*) (*b*)

Figure 2.9 Image of the Palas RBG 1000 (*a*) and diagram of the rotating brush (*b*). [Palas GmbH, 2002]

2.4 Aerosol Characteristics

2.4.1 Selection of Surrogates

Cerium oxide was chosen as the surrogate for spent nuclear fuel ($\rho_{SNF} \approx 10$ g/cm^3) because of its relatively high density ($\rho_{CeO2} = 7.22$ g/cm^3) and its commercial availability. For CeO_2, an AED particle size of 10 µm equates to a geometric particle size of 3.72 µm. Geometric particle size is used exclusively through the remainder of this report. Figure 2.10 shows the particulate sizes as characterized by the probability distribution function (PDF) and cumulative distribution function (CDF) of the surrogate used in these tests. Here, the distributions are plotted as a function of geometric diameter (bottom) and AED (top). This specific lot of CeO_2 was chosen because the particulates were concentrated in the respirable range (AED < 10 µm). The mass median diameter (MMD) was 2.4 µm (or $MMD_{AED} = 6.4$ µm), the geometric standard deviation (GSD) was 1.9, and ~75% of the particles (by mass) were respirable (AED < 10 µm). Fifty percent of the measured particles have a mass smaller than the MMD (also known as D_{50}), and 50% of the measured particles have a mass that is greater.

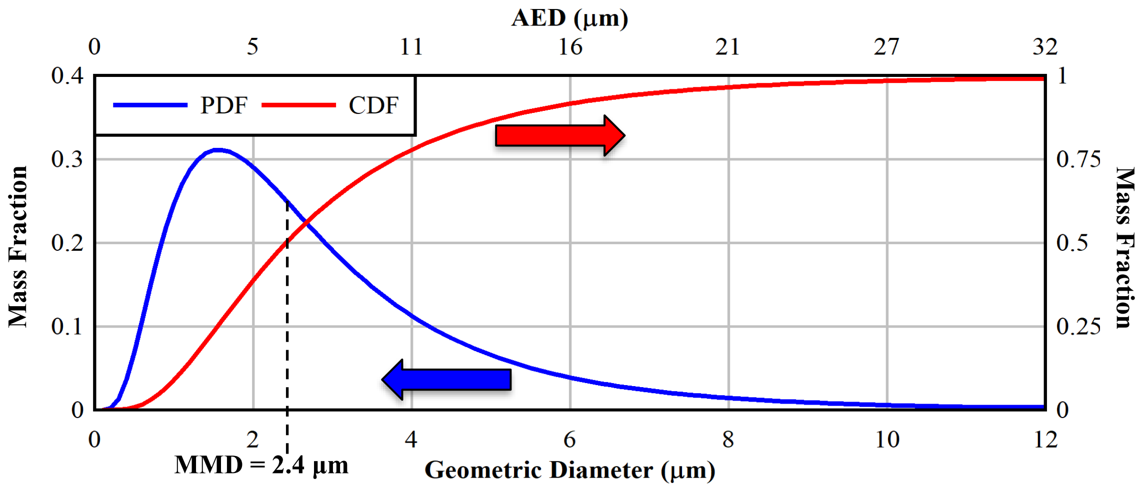

Figure 2.10 Size distributions of the cerium oxide surrogates used in testing.

2.4.2 Reference Initial Aerosol Concentration

The particulates released from SNF were characterized when air was forced through segmented fuel [Hanson *et al.*, 2008]. The geometric particle size data from nine tests conducted on four fuel rod segments are summarized in Figure 2.11. The average of the nine tests yielded an MMD of 3.46 µm (geometric diameter), a GSD of 2.24, a total release fraction of 1.9×10^{-5} of which 46% was respirable for a respirable release fraction of 8.9×10^{-6}. This respirable release fraction is in reasonable agreement with 4.8×10^{-6} cited in NUREG-2125 [NRC, 2012] and 3×10^{-6} cited in SAND90-2406 [Sanders, *et al.*, 1992].

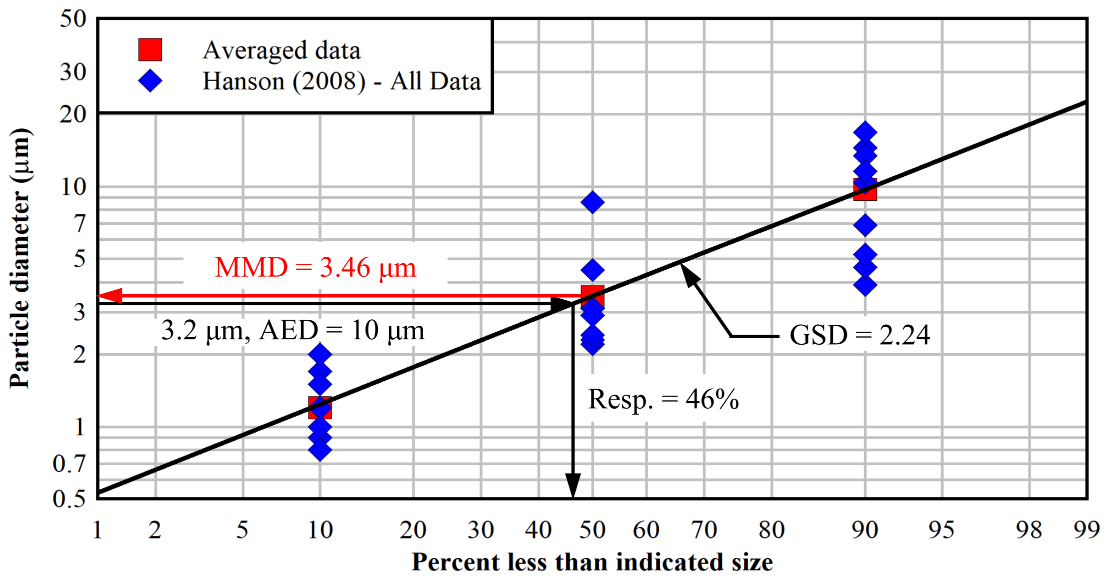

Figure 2.11 Respirable fraction of spent fuel from Hanson *et al.*, 2008.

To estimate an upper aerosol density for spent fuel dry storage, a canister with 37 pressurized water reactor (PWR) assemblies with a uranium oxide (UO_2) fuel mass of 520 kg per assembly was assumed. One percent of the fuel was assumed to fail simultaneously due to an undefined event. The canister was assumed to have an internal free volume of 6 m^3 and a starting initial pressure of 800 kPa (116 psia). The equivalent aerosol density for this assumed system at STP is approximately $C_{m,\,STP} = 54$ mg/m^3. The maximum particle concentration without coincidence error was between 5 and 10 mg/m^3 at STP depending on operating pressure. For all testing described in this report, the standard temperature and pressure were taken as the default values for the mass flow rate instruments (Alicat MC and MW Series) of 298.15 K (25 °C) and 101.353 kPa (14.7 psia).

This page is intentionally left blank.

3 RESULTS

3.1 Clean Flow Tests

The mass flow rate characteristics of the engineered microchannel used in this study were first evaluated in the absence of aerosols. All clean flow tests were conducted with the Promo aerosol sensors off, to allow all gas to exhaust through the microchannel and exhaust pathway. The flow results with air and helium are summarized in Figure 3.1, which shows the air mass flow rate through the clean microchannel as a function of a wide range of pressure drops. Also shown for reference are the initial pressure drops considered in the aerosol-laden tests: nominally 120 kPa, 270 kPa, 420 kPa, 570 kPa, and 720 kPa, indicated in Figure 3.1 by solid black circles. The velocity through the microchannel is roughly the same for both gases at the same pressure differential, but the mass flow rates are significantly different because the density of air is greater than helium by a factor of roughly 7.2 for a given pressure. The average ratio of the measured mass flow of clean air and helium was 7.3 over the range of pressure differential values in Figure 3.1.

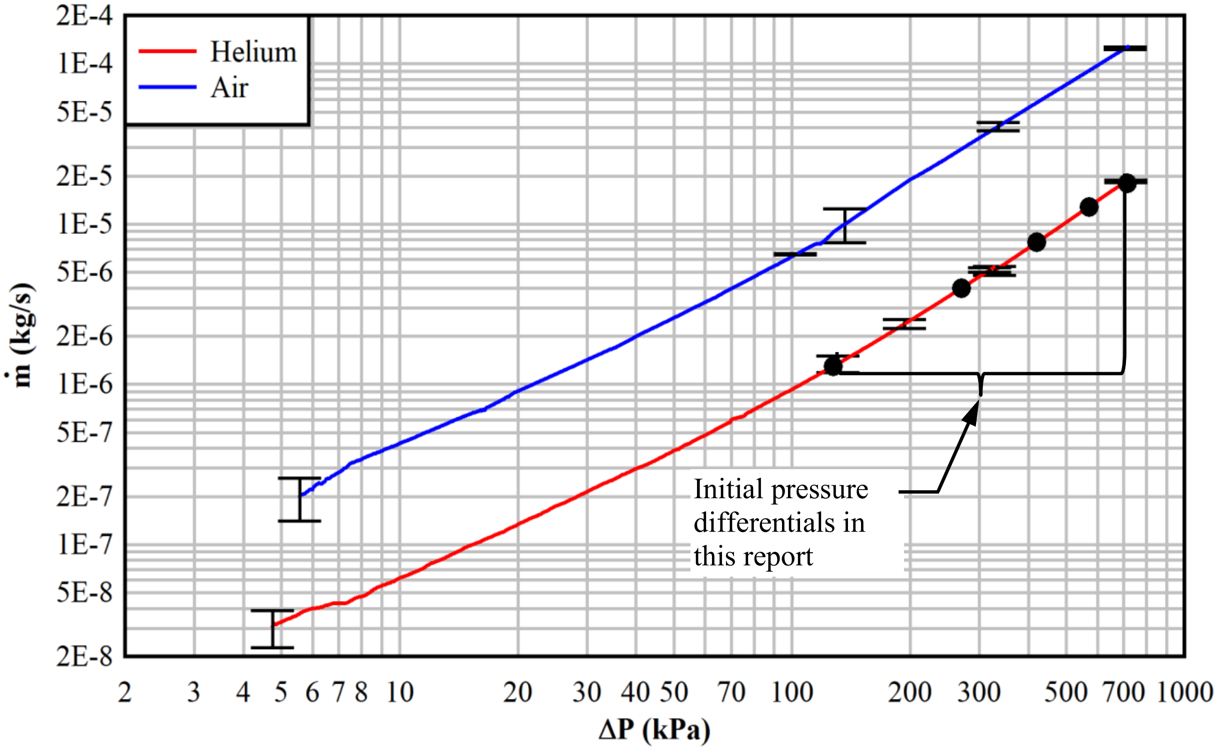

Figure 3.1 Mass flow rate as a function of pressure drop across the linear microchannel for air (blue line) and helium (red line).

3.2 Aerosol-Laden Flow Tests

3.2.1 Air Tests

As summarized in Table 3.1, a total of 18 constant pressure tests with five nominal pressure differentials (120, 270, 420, 570, and 720 kPa) were conducted in FY22 over a range of initial aerosol mass concentrations. The majority of the mass concentrations ranged from 18.7 to 60.4 mg/m^3; one high mass concentration test at 128.2 mg/m^3 was also conducted. Results for the air tests are plotted in Figure 3.2(*a*). The final, integrated aerosol mass, M(τ), in the upstream and downstream sections are given for each test.

The ratio of these values is reported as the integrated transmission. The methods for determining these values are defined in Section 3.2.3.

Table 3.1 Aerosol-laden flow test matrix summary of results for air.

			Upstream Initial Conditions				Final		
Date	Nominal Pressure (bar)	ΔP_o (kPa)	C_m (mg/m^3)	$C_{m,\,STP}$ (mg/m^3)	MMD (µm)	GSD (µm)	M_{Up} (mg)	M_{Down} (mg)	Integrated Transmission
3/23/2022	2.0	119	34.4	17.0	1.7	2.1	0.31	0.12	0.40
3/23/2022	2.0	119	27.4	13.7	1.4	2.1	0.36	0.15	0.41
3/24/2022	2.0	120	22.3	11.1	1.5	1.9	0.28	0.10	0.37
4/8/2022	2.0	123	18.7	9.1	1.5	1.9	0.35	0.16	0.46
4/4/2022	3.5	267	26.9	7.7	1.7	2.0	0.71	0.42	0.60
4/4/2022	3.5	268	37.4	10.7	2.0	2.0	0.66	0.38	0.57
4/5/2022	3.5	267	21.5	6.1	1.4	2.0	0.72	0.45	0.62
3/24/2022	5.0	416	38.1	7.6	1.9	2.1	1.06	0.54	0.51
3/29/2022	5.0	417	19.9	4.0	1.4	1.9	1.04	0.43	0.41
3/30/2022	5.0	418	28.8	5.7	1.8	2.0	1.18	0.51	0.43
4/7/2022	5.0	417	59.6	12.0	2.0	2.0	1.58	0.80	0.50
3/30/2022	6.5	568	37.1	5.7	1.8	2.0	1.55	0.52	0.33
3/31/2022	6.5	567	60.4	9.3	2.2	2.1	2.08	0.62	0.30
4/1/2022	6.5	568	35.3	5.4	2.0	2.1	1.34	0.39	0.29
3/25/2022	8.0	715	33.6	4.2	1.8	2.1	1.50	0.43	0.29
3/28/2022	8.0	715	31.3	3.9	1.7	2.1	1.74	0.75	0.43
3/29/2022	8.0	716	40.4	5.1	1.9	2.1	1.85	0.79	0.43
4/6/2022	8.0	716	128.2	16.1	2.0	2.0	8.11	1.65	0.20

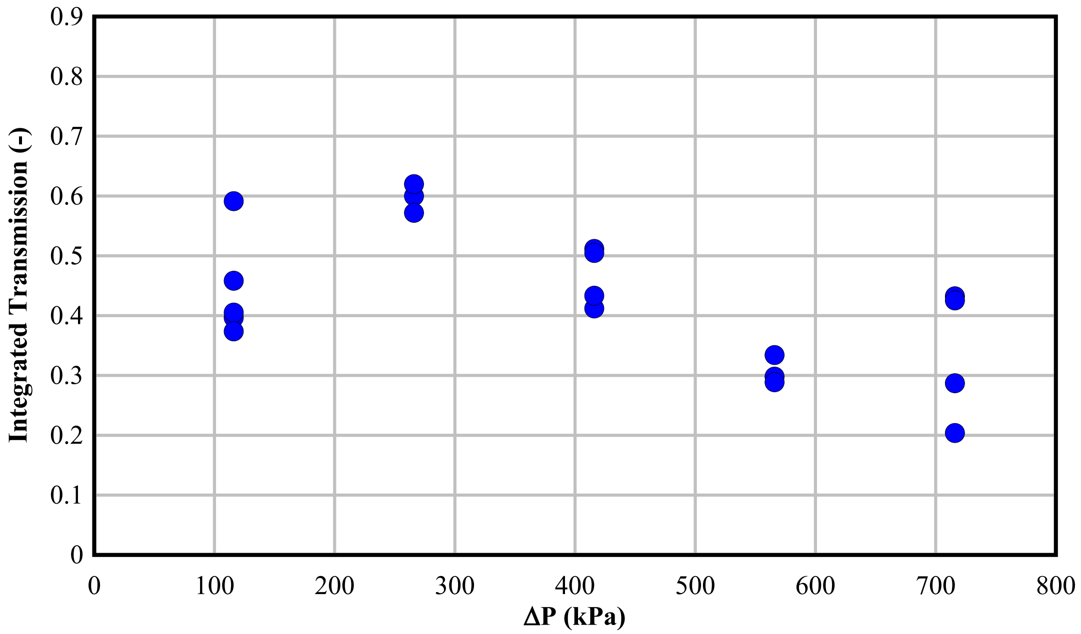

Figure 3.2 Integrated transmission as a function of pressure differential with dry air as the carrier gas.

3.2.2 Helium Tests

A total of 19 constant pressure aerosol-laden helium flow tests were conducted with five nominal pressure differentials (120, 270, 420, 570, and 720 kPa) over a range of initial upstream aerosol concentrations from 9.8 to 41.3 mg/m^3 and is are summarized in Table 3.2. Results for the helium tests are plotted in Figure 3.2(*b*). Combined analyses of the air and helium results are available in Section 3.2.4.

Table 3.2 Aerosol-laden flow test matrix summary of results for helium.

			Upstream Initial Conditions				Final		
Date	**Nominal Pressure (bar)**	**ΔP_o (kPa)**	**C_m (mg/m^3)**	**$C_{m, STP}$ (mg/m^3)**	**MMD**	**GSD**	**M_{Up} (mg)**	**M_{Down} (mg)**	**Integrated Transmission**
4/14/2022	2.0	119	22.0	11.0	1.1	2.0	0.3	0.0	0.12
4/21/2022	2.0	123	16.5	8.2	1.2	1.8	0.3	0.0	0.10
4/27/2022	2.0	118	10.9	5.5	1.0	1.8	0.3	0.0	0.10
4/25/2022	3.5	249	26.9	7.7	1.4	1.9	0.8	0.5	0.64
4/26/2022	3.5	266	15.7	4.5	1.2	1.8	1.0	0.6	0.63
4/26/2022	3.5	268	17.7	5.1	1.1	1.8	0.9	0.3	0.31
7/21/2022	3.5	266	19.4	5.6	1.2	2.9	0.7	0.4	0.65
8/1/2022	3.5	266	41.3	11.9	1.7	2.0	1.1	0.7	0.65
8/2/2022	3.5	266	18.8	5.4	1.1	1.8	0.9	0.7	0.76
8/3/2022	3.5	266	25.5	7.4	1.4	1.8	1.1	0.5	0.49
4/20/2022	5.0	424	20.5	4.1	1.2	1.9	1.0	0.7	0.64
4/21/2022	5.0	417	9.8	2.0	0.9	1.8	1.0	0.7	0.71
4/22/2022	5.0	424	19.8	4.0	1.3	1.9	0.8	0.7	0.83
4/15/2022	6.5	566	28.7	4.4	1.7	2.0	1.3	0.8	0.60
4/19/2022	6.5	568	24.6	3.8	1.6	2.1	1.1	0.8	0.68
4/19/2022	6.5	566	30.3	4.7	1.7	1.8	1.3	0.8	0.59
7/19/2022	6.5	566	27.8	4.3	1.5	1.9	1.9	0.9	0.46
7/20/2022	6.5	565	28.1	4.4	1.5	2.0	1.9	0.6	0.33
4/12/2022	8.0	717	31.5	3.9	1.6	2.0	1.6	0.7	0.46
4/13/2022	8.0	717	27.8	3.5	1.4	2.1	1.8	0.9	0.50
4/14/2022	8.0	717	26.4	3.3	1.4	2.0	1.6	0.8	0.52

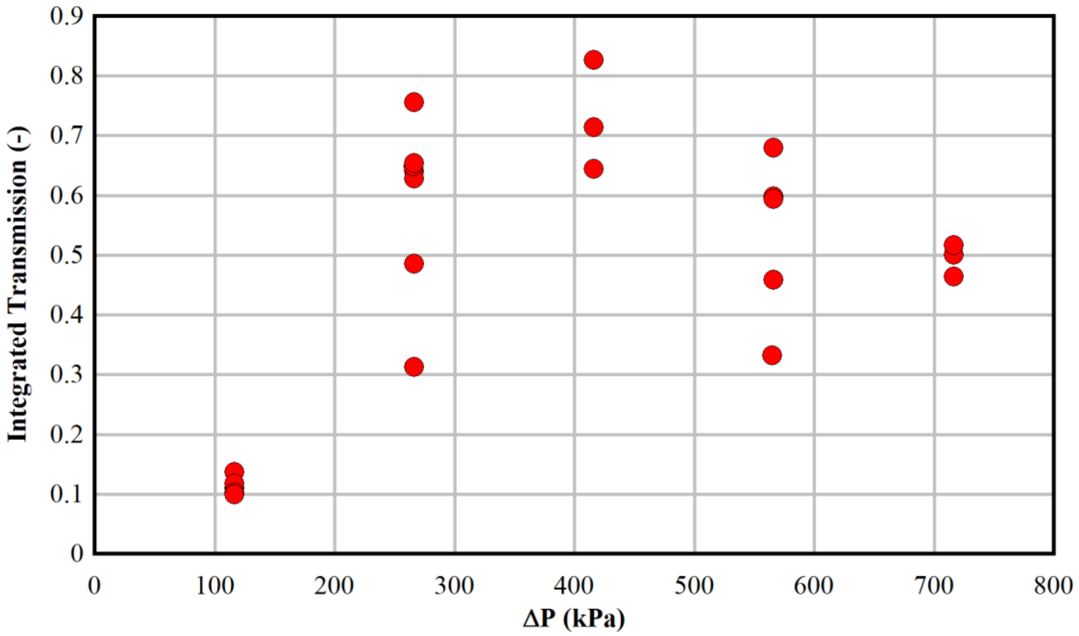

Figure 3.3 **Integrated transmission as a function of pressure differential with helium as the carrier gas.**

3.2.3 Data Analysis

The measured instantaneous mass rate of aerosols upstream or downstream of the microchannel at any time *t* may be expressed as shown in Equation 3.1. Here, the mass flow rate of the background gas, Q_{STP} in units of m^3/s, at time *t* is multiplied by the mass concentration of aerosols, $C_{m,\,STP}$ in units of mg/m^3, at the same time *t*, both at STP conditions. The instantaneous transmission at time *t* is defined as the mass rate downstream divided by the corresponding instantaneous mass rate upstream as shown for the complementary instantaneous retention in Equation 3.2. The integrated mass transmitted to and from the microchannel is calculated as the integral of the instantaneous mass rate from a lower limit of $t_o = 0.1$ hours to an upper limit governed by the available aerosol data (τ) as shown in Equation 3.3. The initial offset in the integration limit of 0.1 hours is to account for the short delay in flow of aerosols from the storage tank into the test section. By taking the ratio of the downstream to the upstream integrated mass of aerosols, the integrated transmission of aerosols through the microchannel may be estimated (Equation 3.4). Because the mass flow of gas through the microchannel is conserved in the upstream and downstream calculation in Equation 3.1, the flow cancels in the calculation of the integrated transmission in Equation 3.4. Inherent assumptions are minimal aerosol wall and flow flange impaction losses between the upstream and downstream sample locations and quasi steady-state flow upstream and downstream of the microchannel.

$$\mathrm{m}(t) = \mathrm{Q}_{\mathrm{STP}}(t)\cdot \mathrm{C}_{\mathrm{m,\,STP}}(t)\ \ [\text{Units} = \text{mg/s}] \tag{3.1}$$

$$\text{Instantaneous Retention} = 1 - \mathrm{m}_{\mathrm{Down}}(t) / \mathrm{m}_{\mathrm{Up}}(t) \tag{3.2}$$

$$\mathrm{M}(\tau) = \int_{t_o}^{\tau} \mathrm{m}(t)\,dt\ \ [\text{Units} = \text{mg}] \tag{3.3}$$

$$\text{Integrated Transmission} = \mathrm{M}_{\mathrm{Down}}(\tau) / \mathrm{M}_{\mathrm{Up}}(\tau) \tag{3.4}$$

3.2.3.1 Aerosol Concentration

Transmission of particulates through the microchannel was determined directly by measuring the aerosol concentration contemporaneously both upstream and downstream of the microchannel. To facilitate this analysis, the raw temporal concentration data were fit to a fourth order log-log polynomial prior to the integration. Figure 3.4 shows an example of the upstream and downstream concentration transients and curve fits for the air blowdown test conducted on March 30, 2022. The upstream aerosol concentration drops nearly two orders of magnitude over seven hours indicating aerosol depletion in the pressure tank. The concentration of aerosol for any given time is greater upstream than downstream indicating the microchannel was acting as a filter. For all tests, the start of the test ($t = 0$ hours) is marked by the opening of the 2 in. ball valve to the storage tank releasing aerosols to the microchannel. An additional, temporal correction was needed to synchronize the samples because of the transit time of the carrier gas from the upstream to the downstream sample ports. This correction was approximated by shifting the downstream data earlier in time based on the time required to displace the volume of gas between the upstream sampling port and the microchannel. The typical time shift was on the order of minutes.

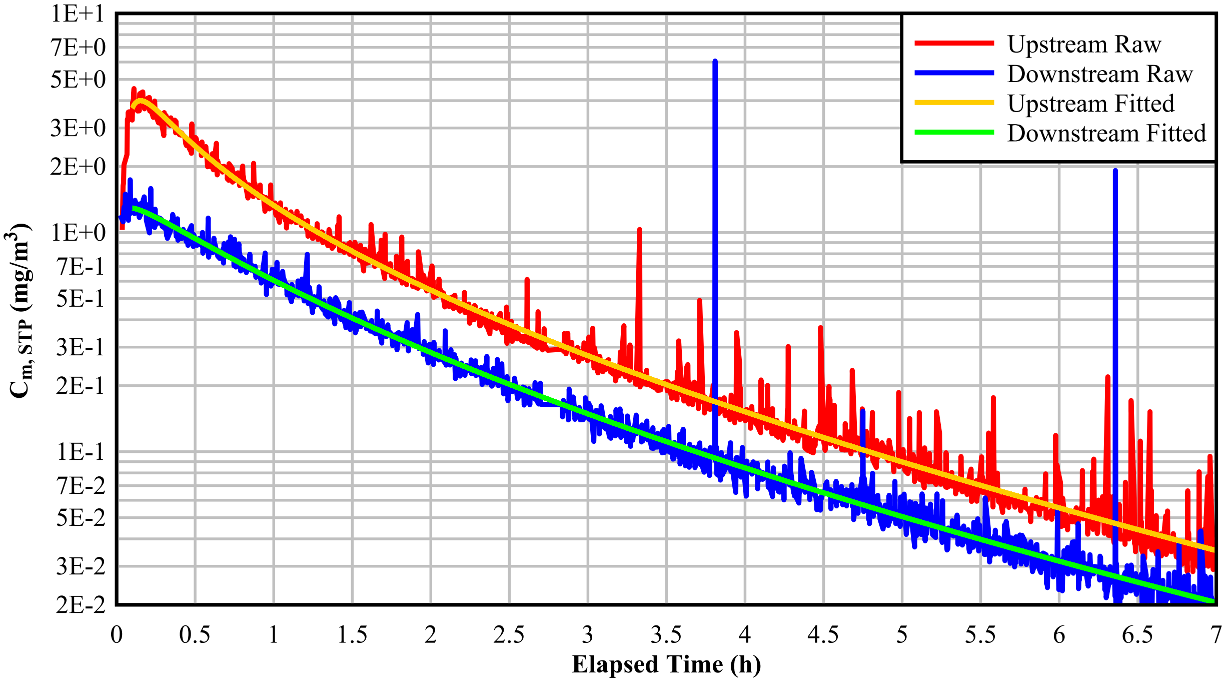

Figure 3.4 Raw and curve-fit aerosol mass concentrations for the constant pressure air test conducted on 03/28/2022 with $\Delta P_o = 715$ kPa and an initial upstream concentration of $C_{m,\,Up,\,STP,\,o} = 3.9$ mg/m^3 ($C_{m,\,Up,\,o} = 31.3$ mg/m^3).

Figure 3.5 shows a typical result of the integrated aerosol masses for the upstream and downstream sections on the left dependent axis for the test conducted on March 28, 2022. The ratio of the downstream to the upstream aerosol mass, *i.e.* integrated transmission, is shown on the right dependent axis. Although care was taken to accommodate the stabilization of the aerosol concentrations at the start of the test, the combination of curve fitting and the selection of a test-independent lower integration limit, $t_o = 0.1$ h, led to some integrated transmissions displaying initial, non-monotonic behavior at elapsed times less than half an hour.

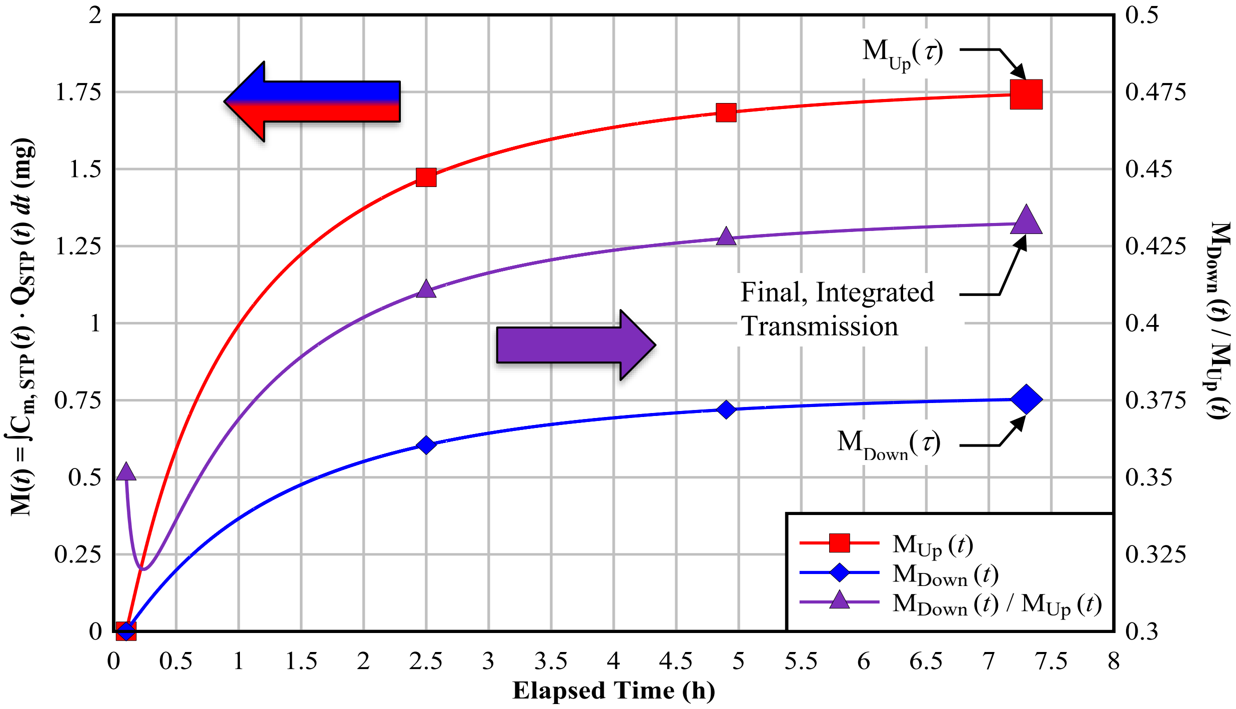

Figure 3.5 Integrated aerosol mass concentrations for the constant pressure air test conducted on 03/28/2022 with $\Delta P_o = 716$ kPa and an initial upstream concentration of $C_{m,\,Up,\,STP,\,o} = 3.9$ mg/m^3 ($C_{m,\,Up,\,o} = 31.3$ mg/m^3).

Figure 3.6 shows how the particle distribution upstream and downstream of the crack changes throughout the course of a test. Upstream, the particle diameters appear to decay which is likely due to gravitational settling of larger particles. The difference between the upstream and downstream 84th percentile is greater than the 50th and 16th indicating that the crack is more effective at filtering larger particles than smaller ones. The transient upstream and downstream particle size distributions are recorded for each test.

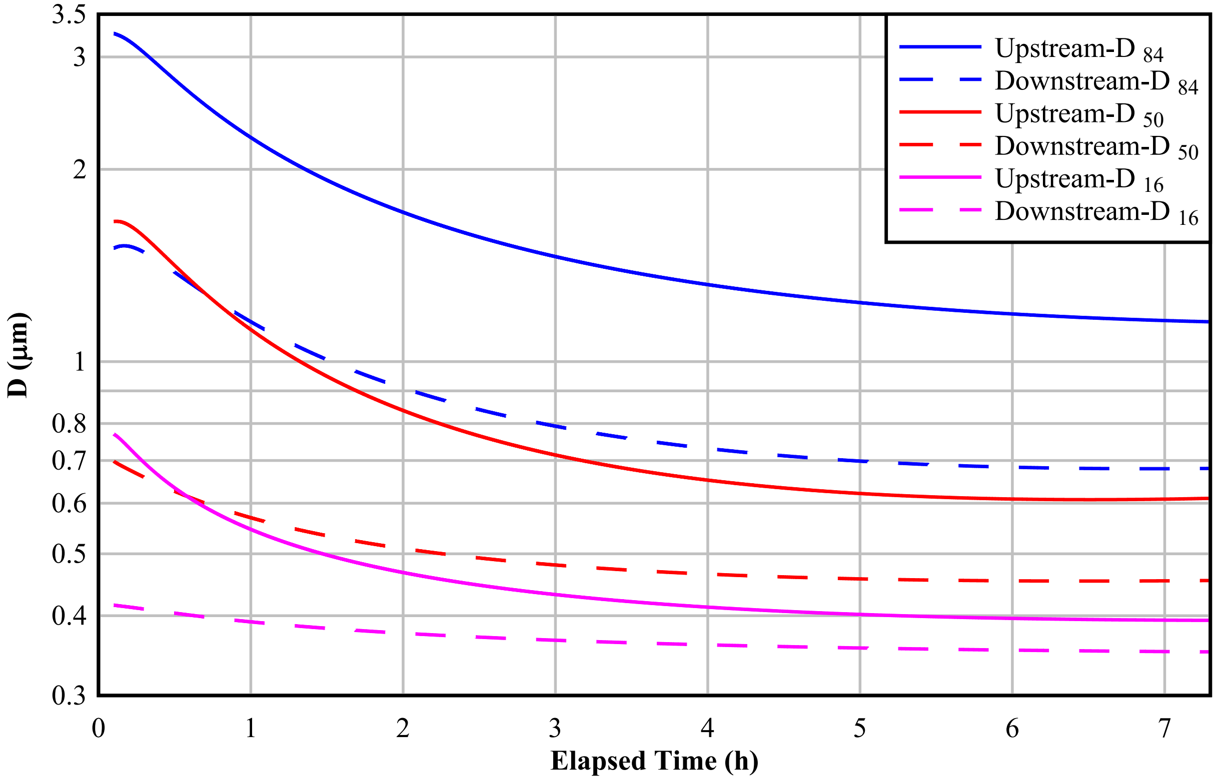

Figure 3.6 Particle diameter of the 84th, 50th, and 16th percentile by mass for the constant pressure air test conducted on 03/28/2022 with $\Delta P_o = 716$ kPa and an initial upstream concentration of $C_{m,\,Up,\,STP,\,o} = 3.9$ mg/m^3 ($C_{m,\,Up,\,o} = 31.3$ mg/m^3).

3.2.4 Comparison of Air and Helium Aerosol Transmissions

The transmission behavior of the aerosols suspended in air and helium for FY22 testing are very similar. Figure 3.7 shows the measured transmission of aerosol mass through the linear slot orifice as a function of the initial MMD_o for both air and helium used as the fill gas. Air tests (blue symbols) and helium tests (red symbols) are shown together in the. The data show an inverse relationship such that the transmission is high when the MMD_o is small, and the transmission is low when the MMD_o is large. This behavior is observed for both fill gases tested at most differential pressures. The seemingly repeatable exception to this is the 120 kPa helium tests which required the use of a cover gas in the exhaust portion of the test section. Without the cover gas, the sample flow would be contaminated with atmospheric air. The cover gas dilutes the aerosol sample and was accounted for in data processing, but the reduction in transmission persists. It is possible that because flow comes from both upstream and downstream of the sample port, there may be some stagnation downstream of the crack that allows for settling of some particles. The integrated transmission appears to be independent of carrier gas, and while more testing is needed to verify this, the potential to conduct the majority of tests with air is highly attractive because of experimental ease and cost.

The estimated particle size distribution from spent fuel testing $MMD_o = 3.46$ µm [Hanson *et al.*, 2008] has proven to be difficult to achieve with the current experimental set-up and procedure. The larger particles deplete from the distribution more quickly than the smaller particles, so the interval of time between initial tank seeding and the start of the test (opening the 2-in. ball valve) can have an impact on the initial upstream particle size distribution. Every effort is made to minimize this duration, but there exists a practical limit due to the required calibration procedure at operating pressure, and the maximum

200 kPa operating pressure of the RBG. Increased mixing in the pressure tank could help keep the larger particles suspended for longer, but overly aggressive agitation in the tank could disturb conditions immediately upstream of the crack and introduce turbulence that would not be representative of flow through a SCC in a DPC.

In order to better apply the techniques developed for these studies to the hypothetical transmission of fuel particulates through an SCC, future work must consider the expected aerosol depletion within the canister and other transient factors on the available particulates. To this end, modeling of the canister internals and evolution of aerosols after a release from the fuel to the interior has started in order to inform and synchronize with this research.

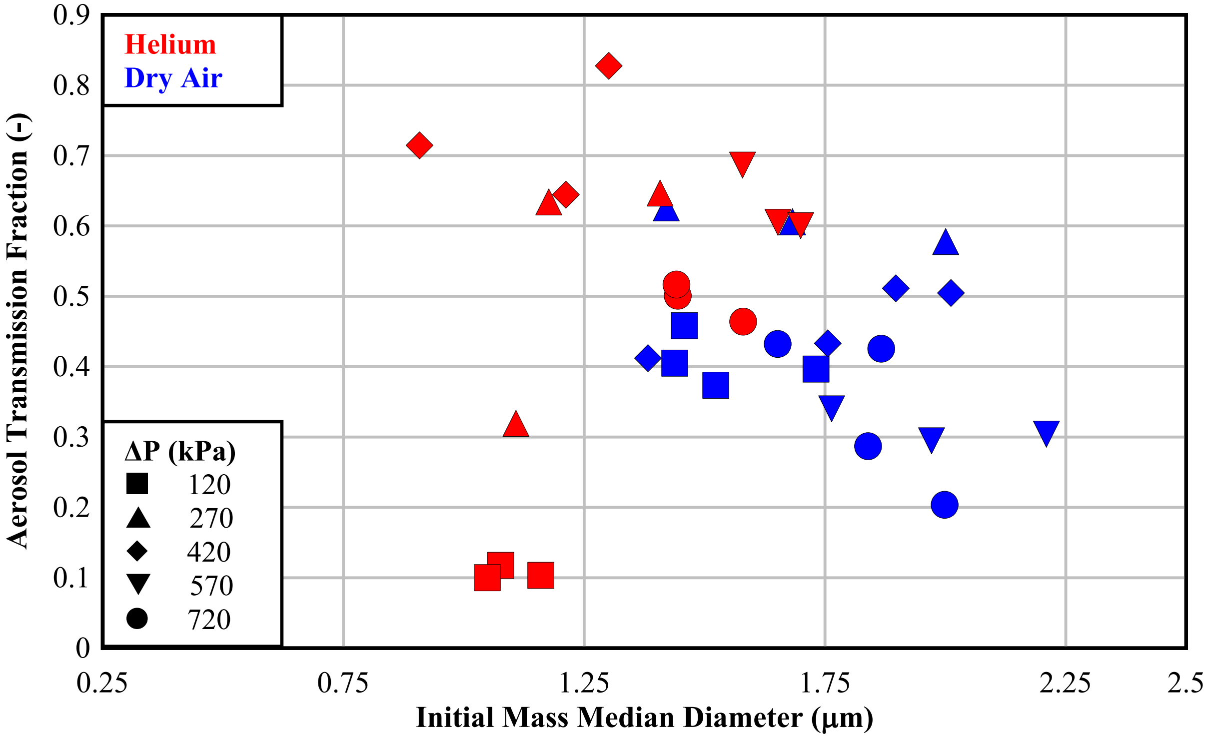

Figure 3.7 **Integrated transmission as a function of initial mass median diameter.**

3.2.5 FY21 versus FY22 Testing Comparison Analysis

The change in calibration procedure discussed in Section 2.3.4 resulted in distinct changes in the results between FY21 and FY22 testing. It was most noticeable in the decrease in initial MMD with helium as the carrier gas, illustrated in Figure 3.8. The FY21 results indicated there was an unexplained dependence of initial MMD on carrier gas. In actuality this dependence was not physical, but rather it due to the sensitivity of the Welas sensor's measured velocity to operating pressure and carrier gas. The Promo system records the in-sensor velocity for monitoring and diagnostic purposes. Plotted in Figure 3.9 is the recorded in-sensor velocity of the Welas sensor monitoring the pressure tank aerosol concentration as a function of tank pressure. Pressure dependence is clearly illustrated and not linear. Given the sensitivity to both pressure and carrier gas, the effect can likely be attributed to the change in gas density.

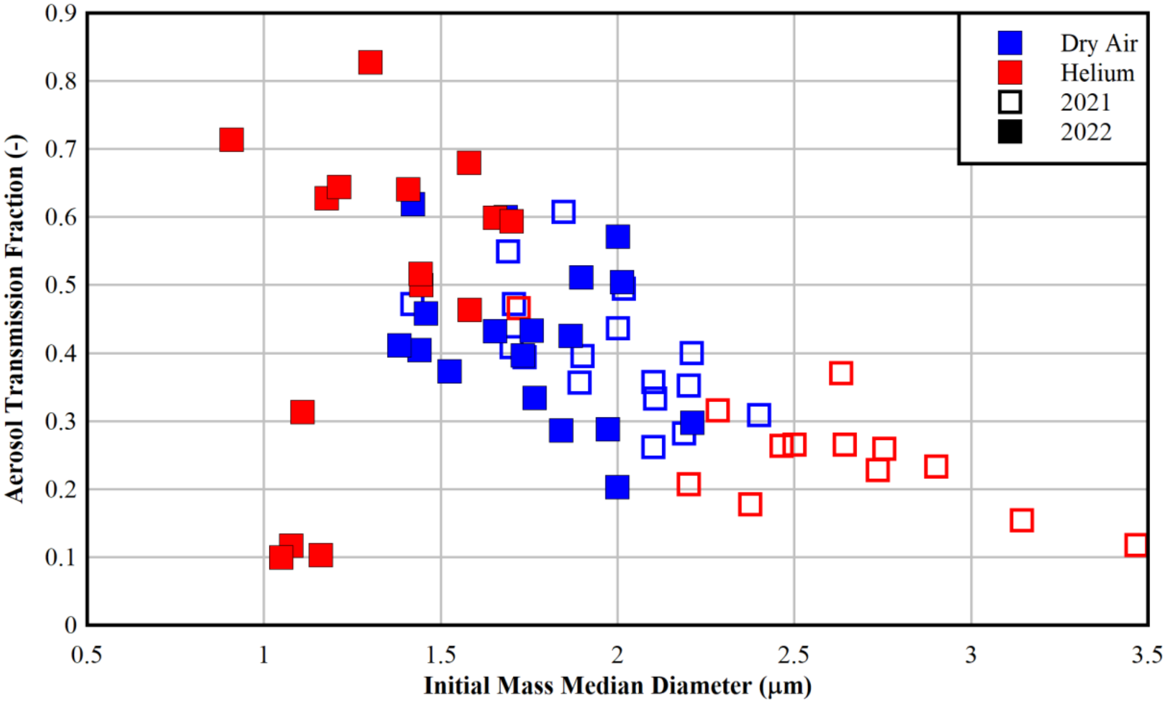

Figure 3.8 Comparison of FY21 and FY22 results, Transmission as a function of initial MMD. Closed symbols are from FY22 and open symbols from FY21.

Cursory examination of Figure 3.9 would suggest there is still carrier gas dependence, but with helium tests producing smaller rather than larger initial MMD. Initial MMD is highly dependent on the amount of time from tank seeding of particles to test initiation – larger particles, which carry the bulk of the mass, settle more rapidly than smaller particles. In general, FY22 testing produced smaller initial MMD than FY21 testing due to the additional at-pressure calibration step which introduced an unavoidable delay from seeding to test initiation. The delay for helium tests was also greater than that of air tests. For reasons unknown, the in-sensor velocity stabilized more rapidly during calibration with air than for helium.

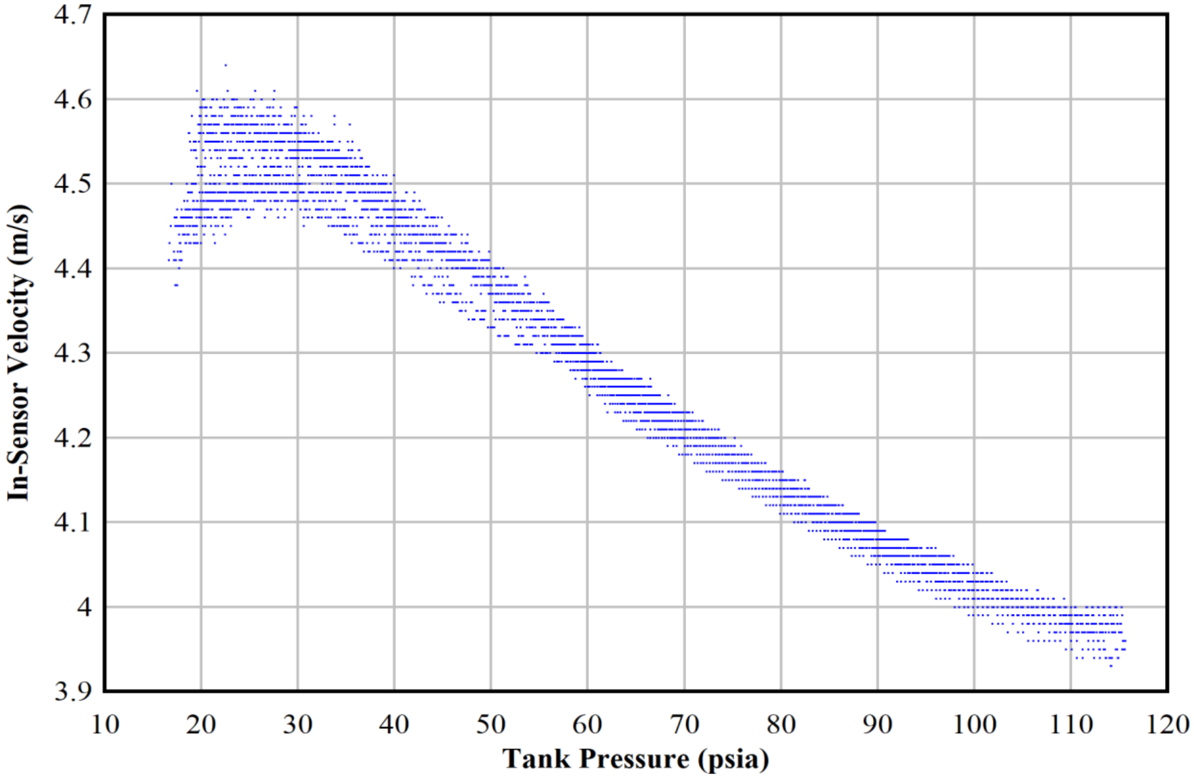

Figure 3.9 Welas in-sensor velocity as a function of tank pressure.

4 SUMMARY

Using a microchannel with an initial cross-section of 12.7 mm × 13 μm tapering linearly to 12.7 mm × 25 μm and a flow length of 8.86 mm, a total of thirty-three aerosol-laden constant pressure tests were conducted at five nominal pressure differentials (120 kPa, 270 kPa, 420 kPa, 570 kPa, and 720 kPa). Tests were conducted with both air and helium as the backfill gas. This microchannel represents the typical dimensions of an SCC albeit without any tortuosity and is therefore a relatively conservative simplification of a hypothetical SCC in a dry storage canister for SNF. The pressure in the tank was maintained through the use of a pressure controller to establish a constant pressure differential across the micro-channel. Previous testing [Durbin *et al*., 2021] showed that because aerosol mass transmission largely occurred at the beginning of the tests, there was no discernable difference in the transmission between the blowdown tests and the tests conducted at constant pressure. As such, current testing has focused on constant pressure tests to decouple the SCC discharge characteristics from the pressure transient.

With the exception of the 120 kPa helium tests, the integrated aerosol transmission varied from roughly 0.20 to 0.83 and appears to be inversely proportional to the initial MMD of the test as shown in Figure 4.1. Deviation in the 120 kPa helium tests could be due to the use of a cover gas. Improvements in the calibration and experimental procedure resulted in lower and less desirable initial MMD compared to previous testing. This shortcoming could be avoided by the procurement of a RBG capable of injecting particles at or above 720 kPa. Further testing is needed to better understand the effect of background gas on the results.

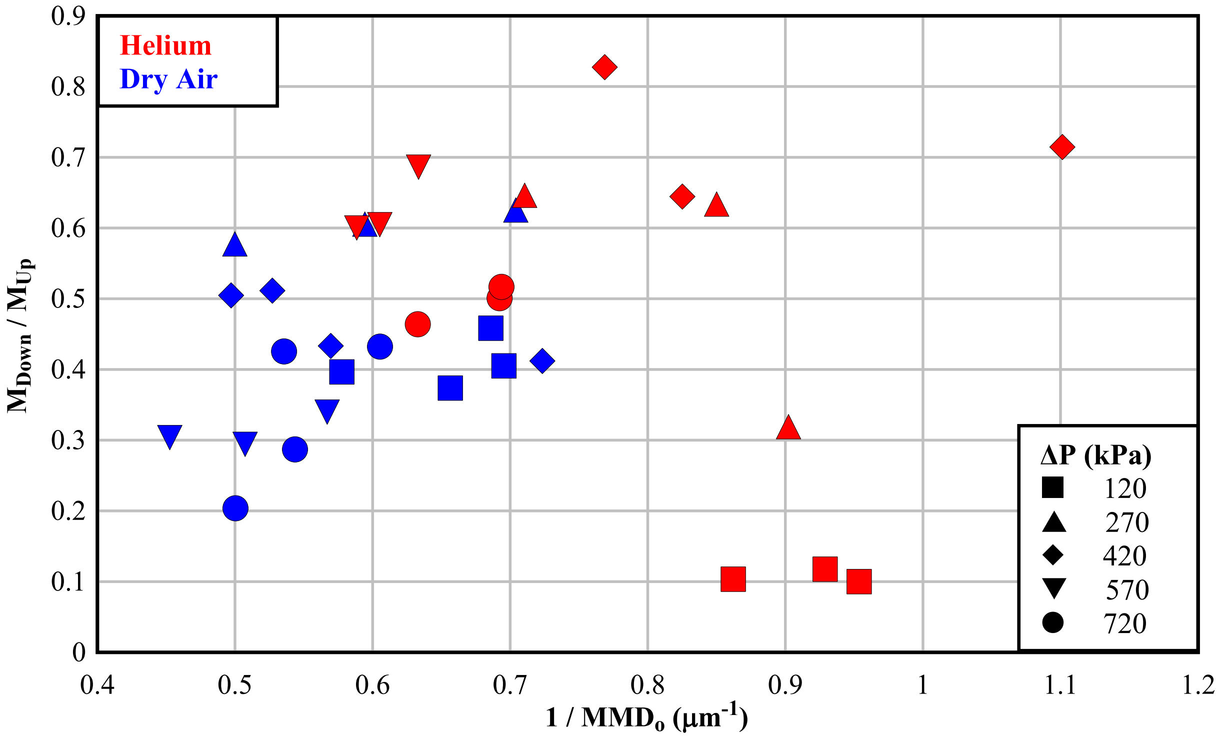

Figure 4.1 **Integrated transmission as a function of the inverse of initial mass median diameter.**

This page is intentionally left blank.

5 REFERENCES

Bixler, N. *et al.*, “State-of-the-Art Reactor Consequence Analyses Project, Volume 1: Peach Bottom Integrated Analysis,” US NRC, NUREG/CR-7110 Vol. 1, Rev. 1, May 2013.

Casella, A., S.K. Loyalka, and B.D. Hanson, “Plugging Effects on Depressurization Time in Dry Storage Containers with Pinhole Breaches,” **Trans. American Nucl. Soc.**, ***95***, 209-210, Washington, D.C., June (2006).

Casella, A., S.K. Loyalka, and B.D. Hanson, “Pinhole Breaches in Spent Fuel Containers: Improvements to Conservative Models of Aerosol Release and Plugging,” **Trans. American Nucl. Soc.**, ***97***, 439-440, Washington, D.C., November (2007).

Chatzidakis, S., and Y. Sasikumar, “Progress Report on Model Development for the Transport of Aerosol through Microchannels,” ORNL/SPR-2020/1599, Oak Ridge National Laboratory, Oak Ridge, Tennessee, April (2021).

Durbin, S.D., E.R. Lindgren and R.J.M. Pulido, “Measurement of Particulate Retention in Microchannel Flows”, SAND2018-10522R, Sandia National Laboratories, Albuquerque, New Mexico, September (2018).

Durbin, S.G., E.R. Lindgren, and A.G. Perales, “Estimation of Respirable Aerosol Release Fractions through Stress Corrosion Crack-Like Geometries,” SAND2020-9014R, M2SF-20SN010207016, Sandia National Laboratories, Albuquerque, New Mexico, August (2020).

Durbin, S.G., R.J.M. Pulido, E.R. Lindgren, P.G. Jones, H. Mendoza, and J. Phillips, “Continued Investigations of Respirable Release Fractions for Stress Corrosion Crack-Like Geometries,” SAND2021-9222R, M2SF-21SN010207071, Sandia National Laboratories, Albuquerque, New Mexico, July (2021).

EPRI, “Flaw Growth and Flaw Tolerance Assessment for Dry Cask Storage Canisters,” EPRI 3002002785 Electric Power Research Institute, Palo Alto, CA, October (2014).

EPRI., “Dry Cask Storage Welded Stainless Steel Canister Breach Consequence Analysis Scoping Study,” EPRI 3002008192, Electric Power Research Institute, Palo Alto, CA, November (2017).

GOTHIC, “Thermal Hydraulic Analysis Package, Technical Manual,” (2018).

Hanson, B.D., R.C. Daniel, A.M. Casella, R.S. Wittman, W. Wu (BSC), P.J. MacFarlan, and R.W. Shimskey, “Fuel-In-Air FY07 Summary Report,” PNNL-17275, Pacific Northwest National Laboratory, Richland, Washington, September (2008).

Humphries L.L., *et al.*, “MELCOR Computer Code Manuals, Vol. 1: Primer and Users’ Guide Version 2.2.11932,” SAND2018-13559 O, November 2018.

Lanza, M., Casella, A., Elsawi, M., Carstens, N., & Springfels, D., “Thermal Hydraulic Modeling of a Dry Cask and Microchannel,” Pacific Northwest National Laboratory Report, PNNL-29225, (2019).

Lanza, M., M. Leimon, M. Elsawi and A. Casella., “GOTHIC Aerosol Source Depletion Studies,” PNNL-31176, M3SF-21PN 010207042, Pacific Northwest National Laboratory, Richland, Washington, April (2021).

Lanza, M., M. Leimon, and A. Casella., “Continued Studies on Aerosol Source Depletion in Dry Spent Nuclear Fuel Storage Canister with GOTHIC,” PNNL-32794, M3SF-22PN010207042, Pacific Northwest National Laboratory, Richland, Washington, April (2022).

Lewis, S., “Solid Particle Penetration into Enclosures”, J. Hazardous Materials, *43,* 195-216, (1995).

Liu, D-L.and W.W. Nazaroff, “Modeling Pollutant Penetration Across Building Envelopes,” **Atmos. Environm.**, ***35***, 4451-4462, (2001).

Liu, D-L. and W.W. Nazaroff, "Particle Penetration Through Building Cracks," **Aerosol Science and Technology**, ***37***, 565-573, (2003).

Meyer, R.M., S. Suffield, E.H. Hirt, J.D. Suter, J.P. Lareau, J.W. Zhuge, A. Qiao, T.L. Moran, and P. Ramuhalli, "Nondestructive Examination Guidance for Dry Storage Casks," PNNL-24412 Rev. 1, Pacific Northwest National Laboratory, Richland, Washington, September (2016).

Mosley, R.B., D.J. Greenwell, L.E. Sparks, Z. Guo, W.G. Tucker, R. Fortmann, C. Whitfield, "Penetration of Ambient Fine Particles into the Indoor Environment," **Aerosol Science and Technology**, ***34***, 127-136, (2001).

Nakos, J.T., "Uncertainty Analysis of Thermocouple Measurements Used in Normal and Abnormal Thermal Environment Experiments at Sandia's Radiant Heat Facility and Lurance Canyon Burn Site," SAND2004-1023, Sandia National Laboratories, Albuquerque, NM, April 2004.

NRC, "Spent Fuel Transportation Risk Assessment," United States Nuclear Regulatory Commission, NUREG-2125, May (2012).

Palas GmbH, "RBG 1000 Particle Generator Manual," Karlsruhe, Germany, (2002).

Phillips, J. and F. Gelbard., "Interim Report on Aerosol Deposition Inside a Spent Fuel Transportation and Storage Canister," SAND2021-5202R, M3SF-21SN010207072, Sandia National Laboratories, Albuquerque, New Mexico, April (2021).

Phillips, J., "MELCOR Input Model for Spent Fuel Transportation and Storage Canister," SAND2022-7306R, M3SFSN010207073, Sandia National Laboratories, Albuquerque, New Mexico, May (2022).

Powers, D.A., "Aerosol Penetration of Leak Pathways – An Examination of the Available Data and Models," SAND2009-1701, Sandia National Laboratories, Albuquerque, NM, April (2009).

Sanders, T.L., K.D. Seager, Y.R. Rashid, P.R. Barrett, A.P. Malinauskas, R.E. Einziger, H. Jordan, T.A. Duffey, S.H. Sutherland, and P.C. Reardon "A Method for Determining the Spent-Fuel Contribution to Transport Cask Containment Requirements," SAND90-2406, Sandia National Laboratories, Albuquerque, NM, November (1992).

Schindelholz, E., C. Bryan, and C. Alexander, "FY17 Status Report: Research on Stress Corrosion Cracking of SNF Interim Storage Canisters," SAND2017-10338R, Sandia National Laboratories, Albuquerque, NM, August (2017).

APPENDIX A TRANSIENT AEROSOL MASS CONCENTRATIONS

Upstream and downstream temporal mass concentrations are presented in this appendix for all tests. The raw data from the Welas 2200 aerosol sensors are plotted alongside the fourth-order log-log polynomial fits to the raw data. For each plot, the start time for the polynomial fits was chosen to be between 0 and 0.1 hours in order to capture as much of the raw data trends as possible. The end time for the polynomial fits was chosen by a logical statement defined by when the downstream test section Welas sensor registers 25 or fewer particles in the ten second measurement period, at which point the analyzed particle number measurements no longer hold statistical significance.

The tests presented in this appendix are defined by the test date, the maintained pressure difference (ΔP), the fill gas (air or helium), and the initial upstream concentration at STP ($C_{m,\,Up,\,STP,\,o}$). The measured initial pressure differential (ΔP_0), and the initial upstream concentration ($C_{m,\,Up,\,o}$) are also provided.

A.1 Air Tests

A.1.1 120 kPa Air

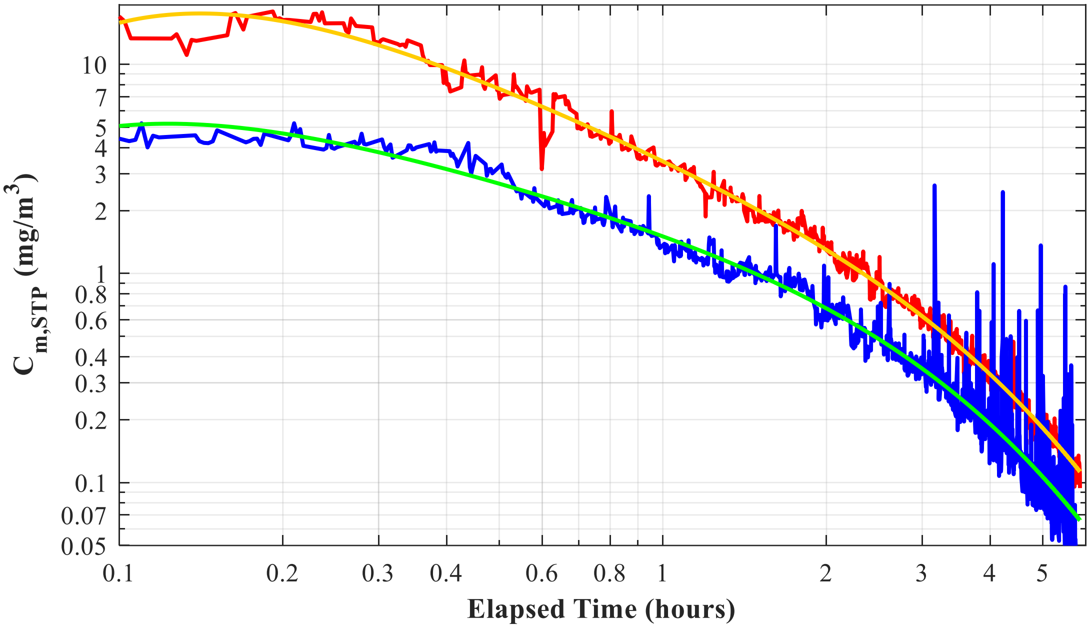

Figure A-1 Raw and curve-fit aerosol mass concentrations for the test on 03/23/2022 with air at constant pressure (ΔP_o = 119 kPa) and an initial upstream concentration of $C_{m,\,Up,\,STP,\,o}$ = 17.0 mg/m^3 ($C_{m,\,Up,\,o}$ = 34.4 mg/m^3).

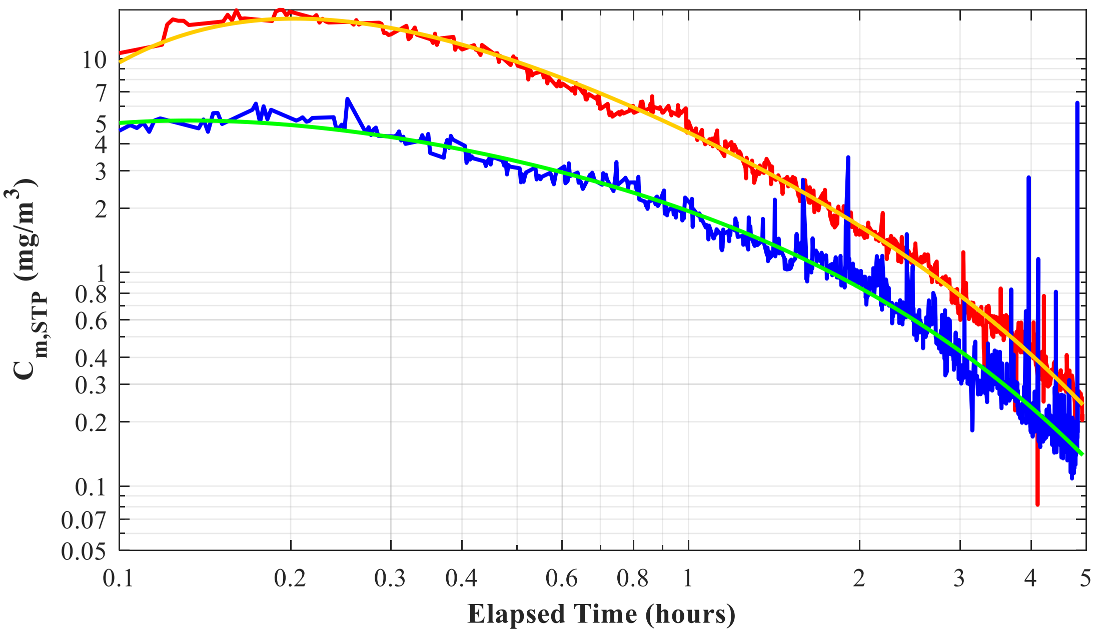

Figure A-2 Raw and curve-fit aerosol mass concentrations for the test on 03/23/2022 PM with air at constant pressure (ΔP_o = 119 kPa) and an initial upstream concentration of $C_{m,\ Up,\ STP,\ o}$ = 13.7 mg/m^3 ($C_{m,\ Up,\ o}$ = 27.4 mg/m^3).

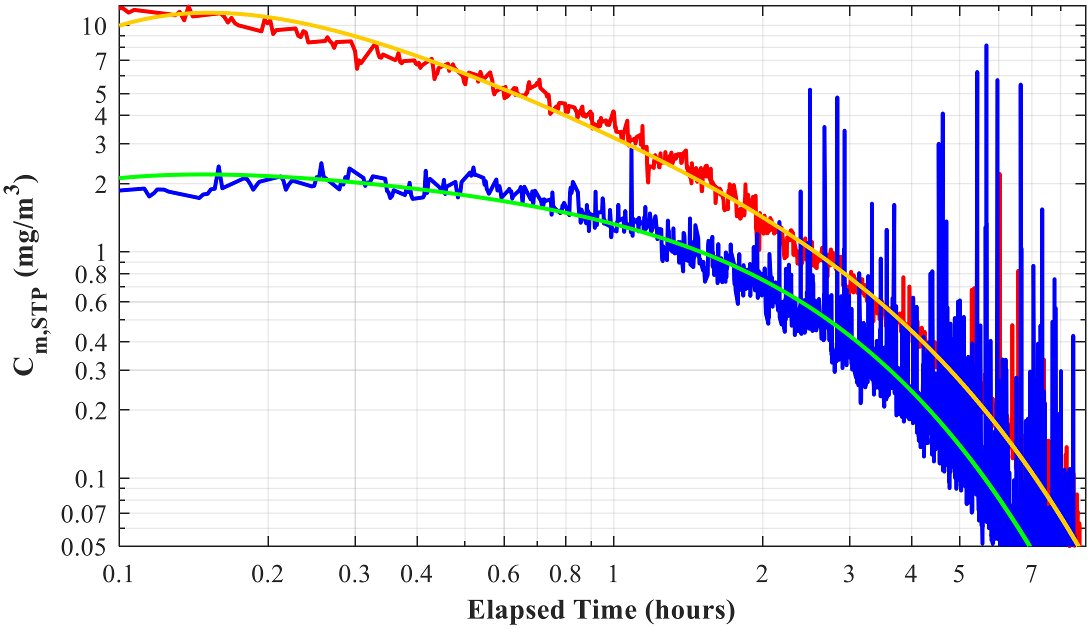

Figure A-3 Raw and curve-fit aerosol mass concentrations for the test on 03/24/2022 with air at constant pressure (ΔP_o = 123 kPa) and an initial upstream concentration of $C_{m,\ Up,\ STP,\ o}$ = 11.1 mg/m^3 ($C_{m,\ Up,\ o}$ = 22.3 mg/m^3).

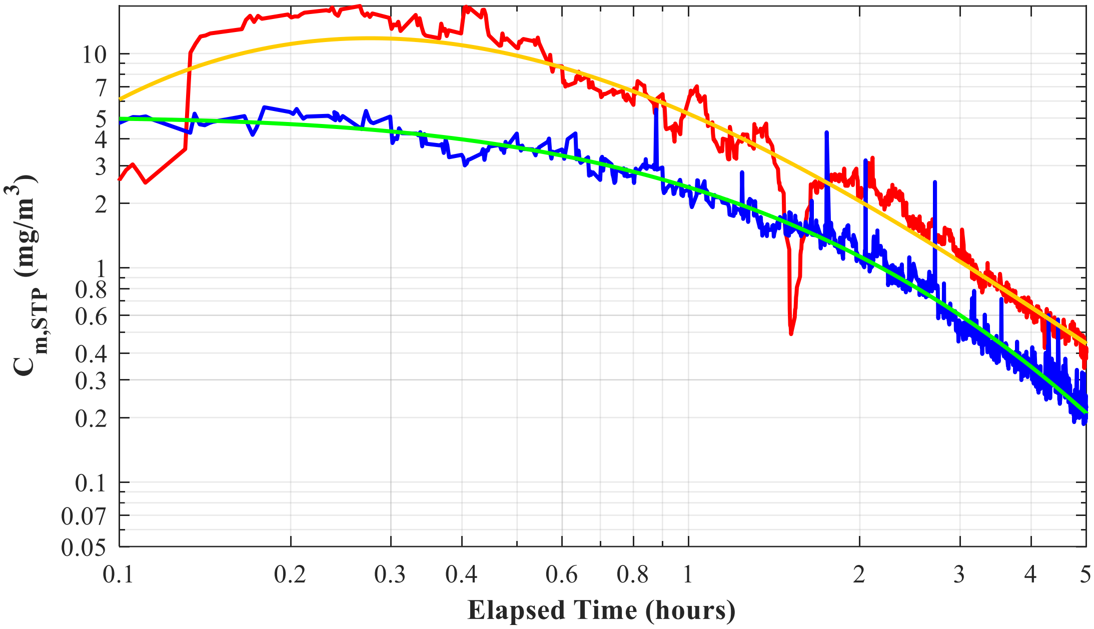

Figure A-4 Raw and curve-fit aerosol mass concentrations for the test on 04/08/2022 with air at constant pressure (ΔP_o = 120 kPa) and an initial upstream concentration of $C_{m,\,Up,\,STP,\,o}$ = 9.1 mg/m^3 ($C_{m,\,Up,\,o}$ = 18.7 mg/m^3).

A.1.2 270 kPa Air

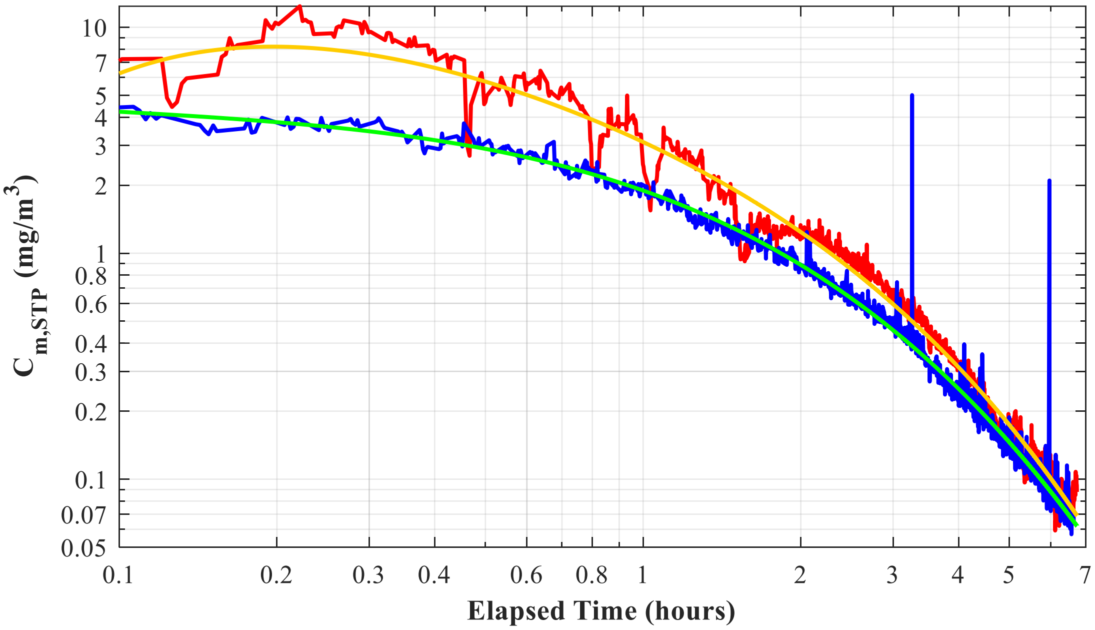

Figure A-5 Raw and curve-fit aerosol mass concentrations for the test on 04/04/2022 with air at constant pressure (ΔP_o = 267 kPa) and an initial upstream concentration of $C_{m,\,Up,\,STP,\,o}$ = 7.7 mg/m^3 ($C_{m,\,Up,\,o}$ = 26.9 mg/m^3).

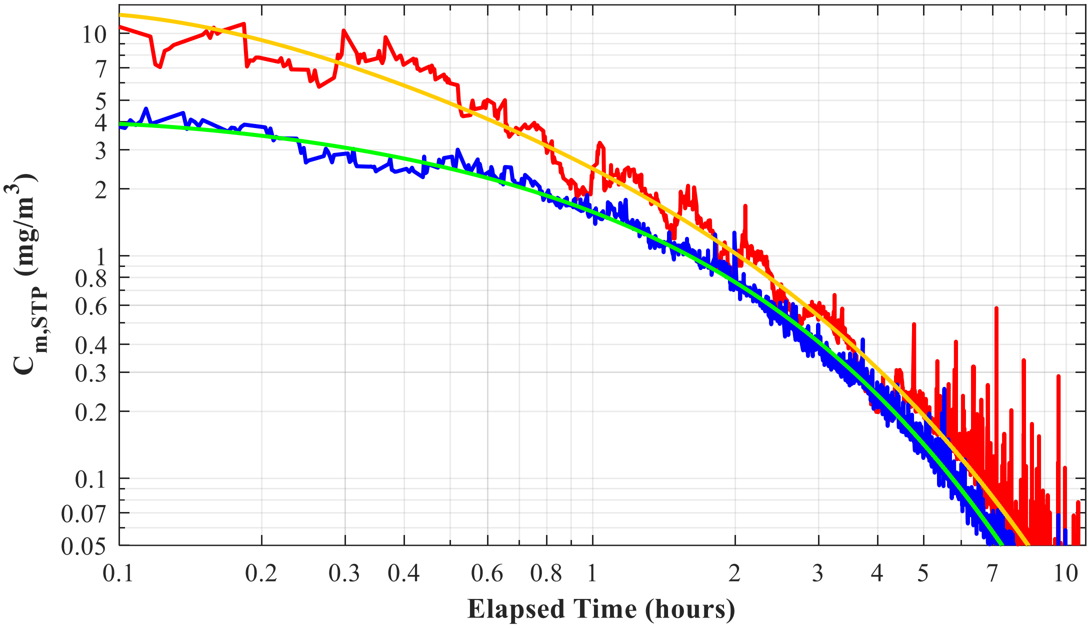

Figure A-6 Raw and curve-fit aerosol mass concentrations for the test on 04/04/2022 PM with air at constant pressure ($\Delta P_o = 268$ kPa) and an initial upstream concentration of $C_{m,\,Up,\,STP,\,o} = 10.7\ mg/m^3$ ($C_{m,\,Up,\,o} = 37.4\ mg/m^3$).

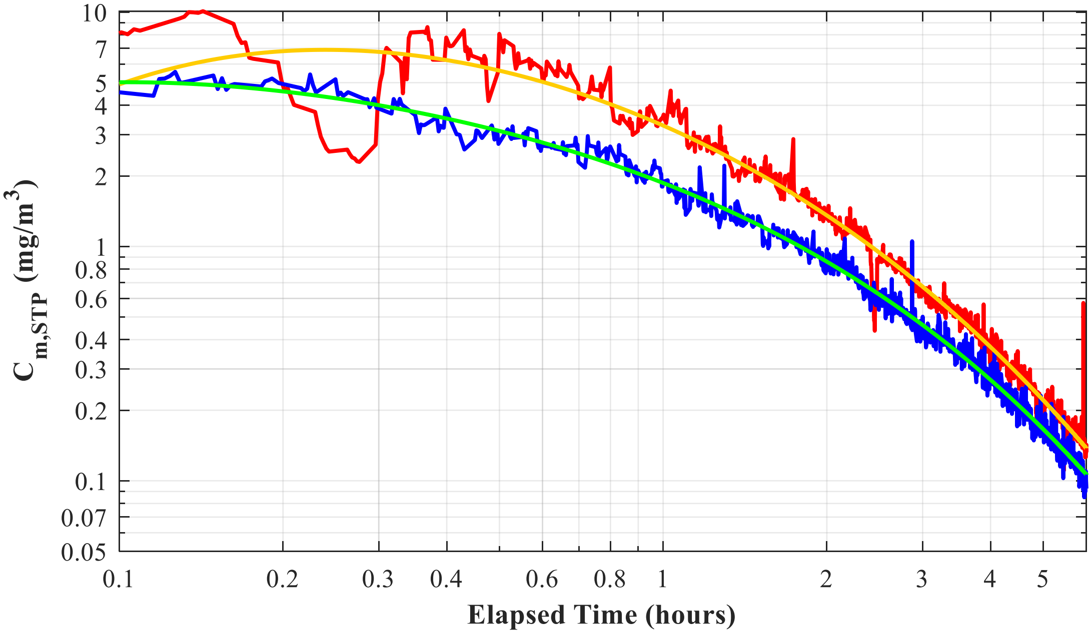

Figure A-7 Raw and curve-fit aerosol mass concentrations for the test on 04/05/2022 with air blowdown from $\Delta P_o = 267$ kPa and an initial upstream concentration of $C_{m,\,Up,\,STP,\,o} = 6.1\ mg/m^3$ ($C_{m,\,Up,\,o} = 21.5\ mg/m^3$).

A.1.3 420 kPa Air

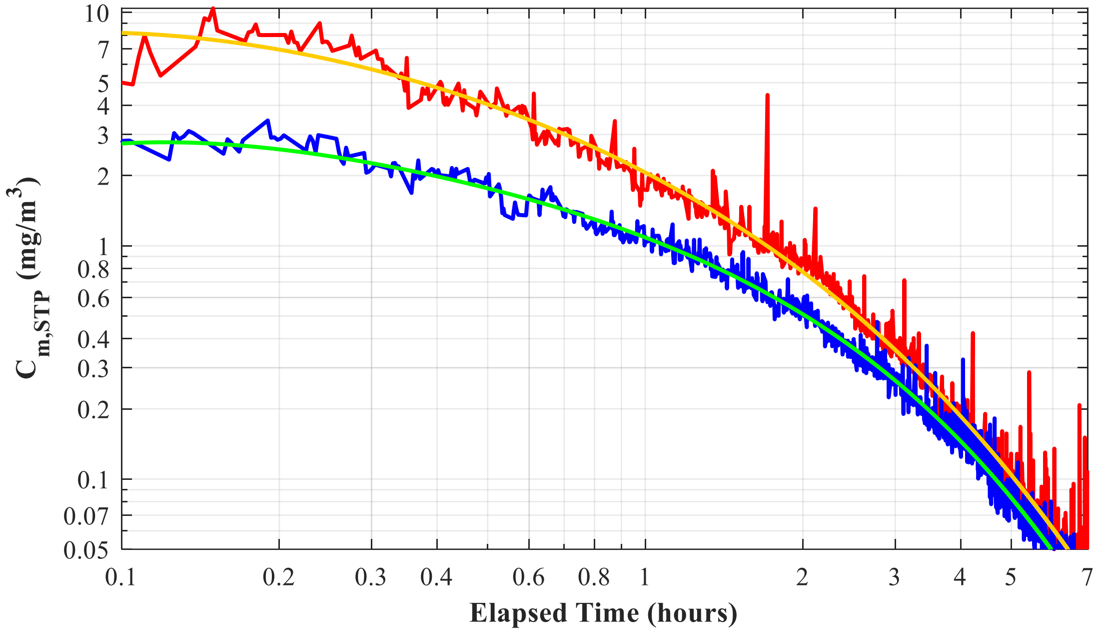

Figure A-8 Raw and curve-fit aerosol mass concentrations for the test on 03/24/2022 with air at constant pressure ($\Delta P_o = 416$ kPa) and an initial upstream concentration of $C_{m,\text{Up},\text{STP},o} = 7.6$ mg/m^3 ($C_{m,\text{Up},o} = 38.1$ mg/m^3).

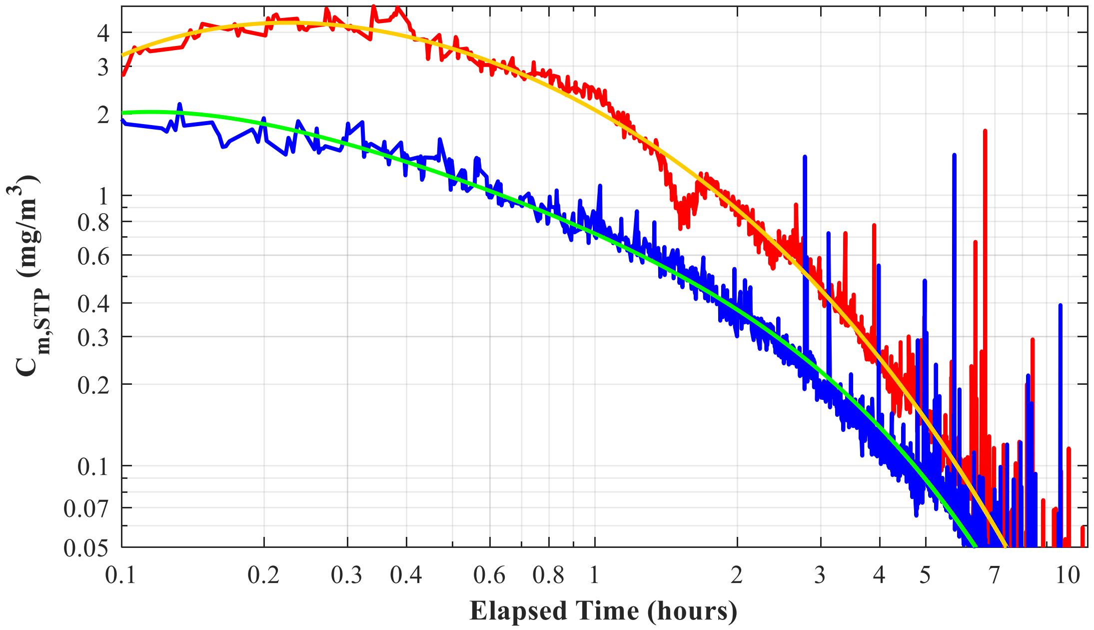

Figure A-9 Raw and curve-fit aerosol mass concentrations for the test on 03/29/2022 with air at constant pressure ($\Delta P_o = 417$ kPa) and an initial upstream concentration of $C_{m,\text{Up},\text{STP},o} = 4.0$ mg/m^3 ($C_{m,\text{Up},o} = 19.9$ mg/m^3).

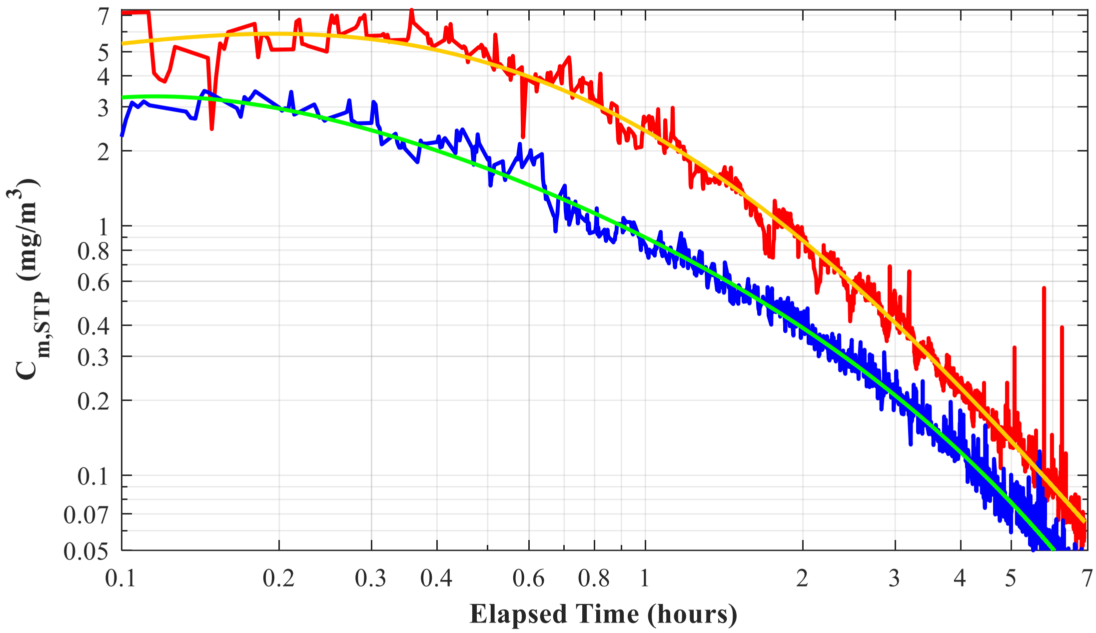

Figure A-10 Raw and curve-fit aerosol mass concentrations for the test on 03/30/2022 with air at constant pressure (ΔP_o = 418 kPa) and an initial upstream concentration of $C_{m,\ Up,\ STP,\ o}$ = 5.7 mg/m^3 ($C_{m,\ Up,\ o}$ = 28.8 mg/m^3).

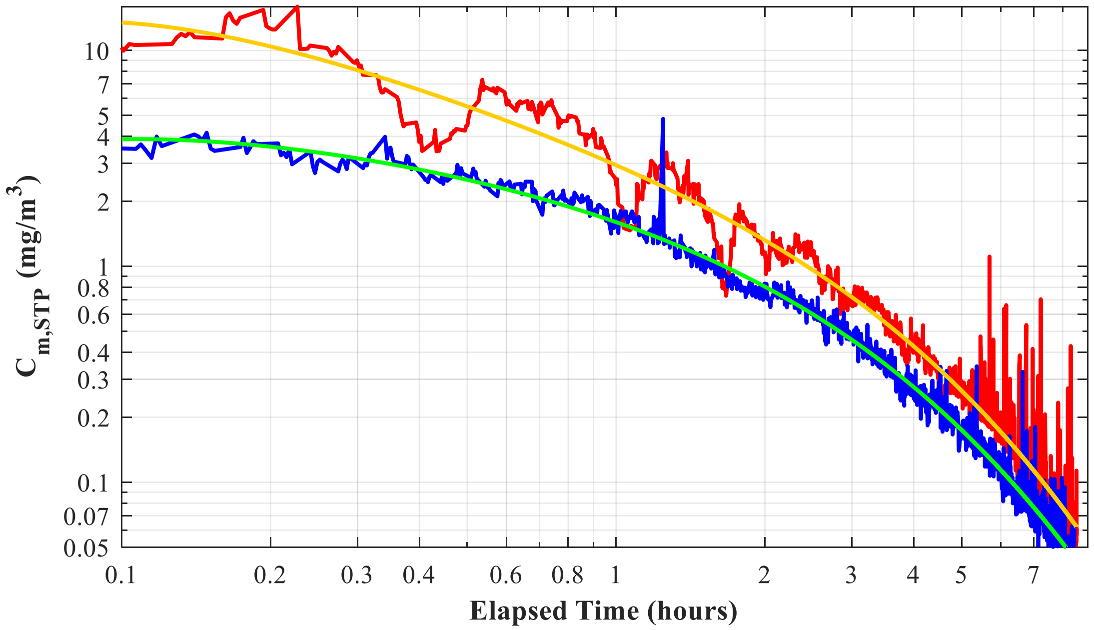

Figure A-11 Raw and curve-fit aerosol mass concentrations for the test on 04/07/2022 with air blowdown from ΔP_o = 417 kPa and an initial upstream concentration of $C_{m,\ Up,\ STP,\ o}$ = 12.0 mg/m^3 ($C_{m,\ Up,\ o}$ = 59.6 mg/m^3).

A.1.4 570 kPa Air

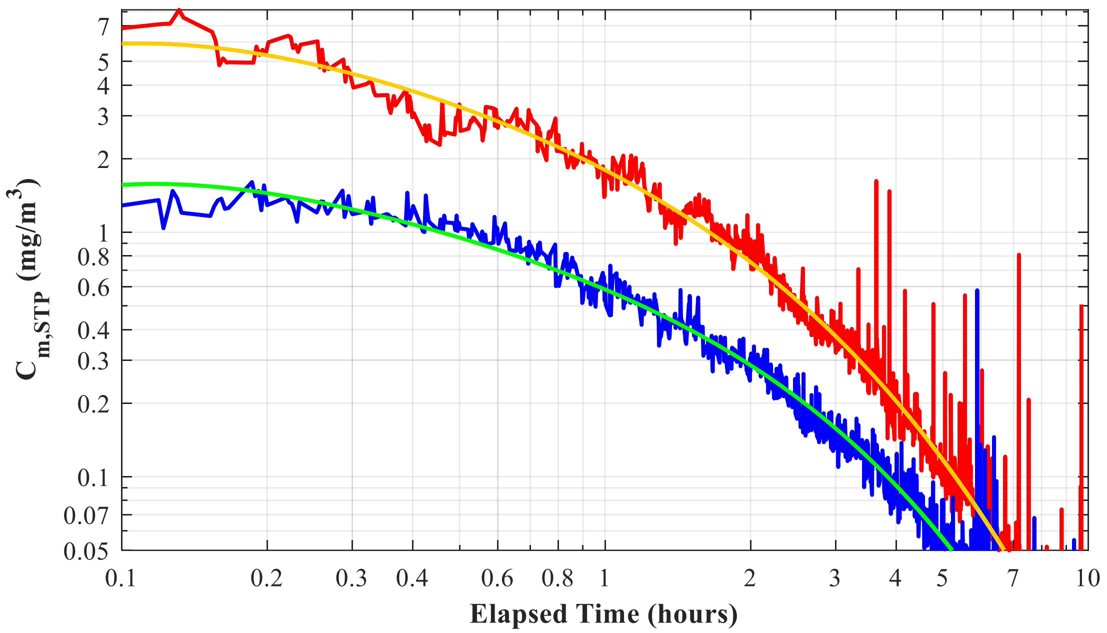

Figure A-12 Raw and curve-fit aerosol mass concentrations for the test on 03/30/2022 with air at constant pressure (ΔP_o = 568 kPa) and an initial upstream concentration of $C_{m,\,Up,\,STP,\,o}$ = 5.7 mg/m^3 ($C_{m,\,Up,\,o}$ = 37.1 mg/m^3).

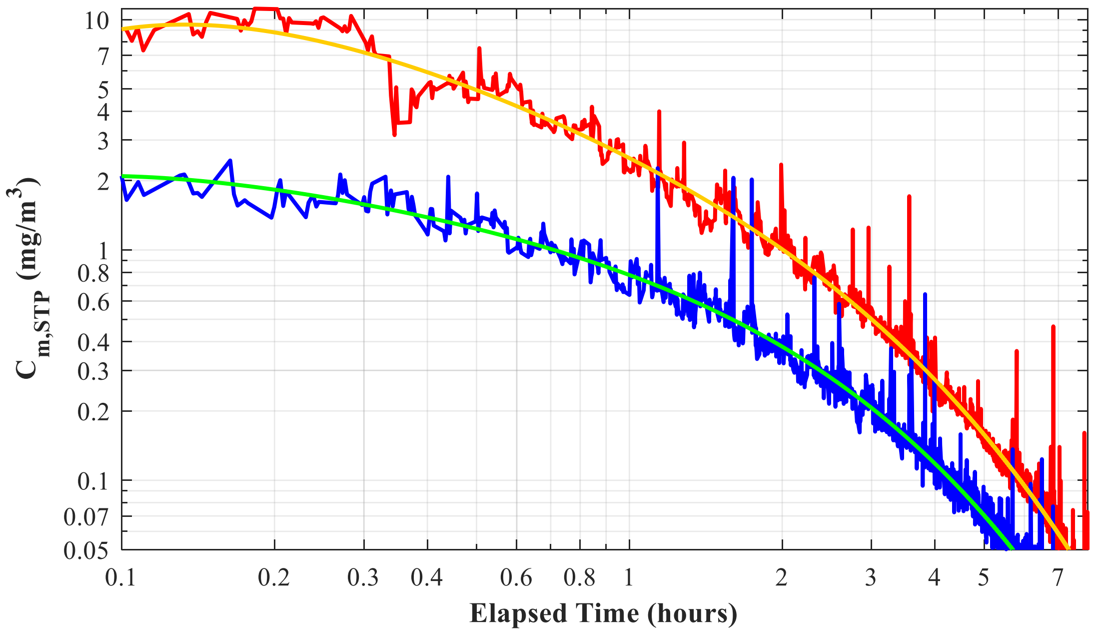

Figure A-13 Raw and curve-fit aerosol mass concentrations for the test on 03/31/2022 with air at constant pressure (ΔP_o = 567 kPa) and an initial upstream concentration of $C_{m,\,Up,\,STP,\,o}$ = 9.3 mg/m^3 ($C_{m,\,Up,\,o}$ = 60.4 mg/m^3).

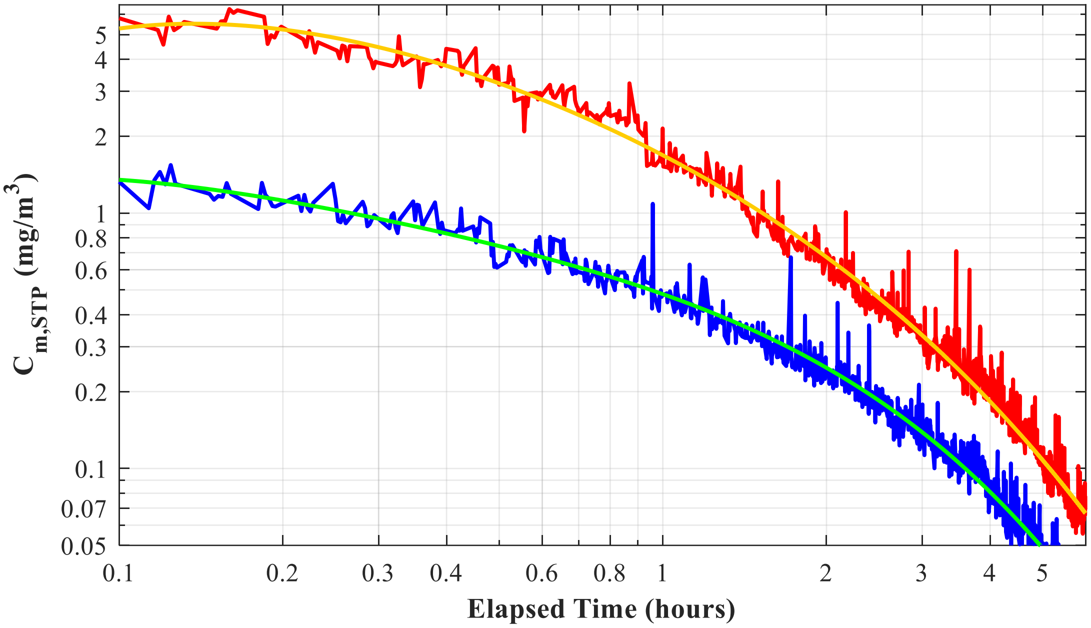

Figure A-14 Raw and curve-fit aerosol mass concentrations for the test on 04/01/2022 with air at constant pressure (ΔP_o = 568 kPa) and an initial upstream concentration of $C_{m,\,Up,\,STP,\,o}$ = 5.4 mg/m^3 ($C_{m,\,Up,\,o}$ = 35.3 mg/m^3).

A.1.5 720 kPa Air

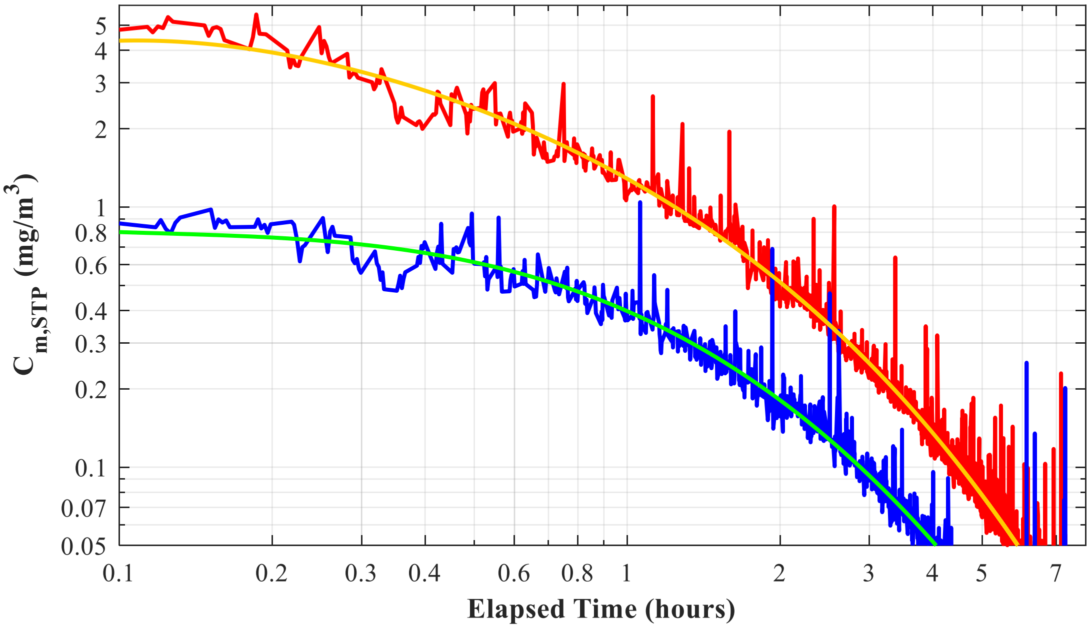

Figure A-15 Raw and curve-fit aerosol mass concentrations for the test on 03/25/2022 with air at constant pressure (ΔP = 715 kPa) and an initial upstream concentration of $C_{m,\,Up,\,STP,\,o}$ = 4.2 mg/m^3 ($C_{m,\,Up,\,o}$ = 33.6 mg/m^3).

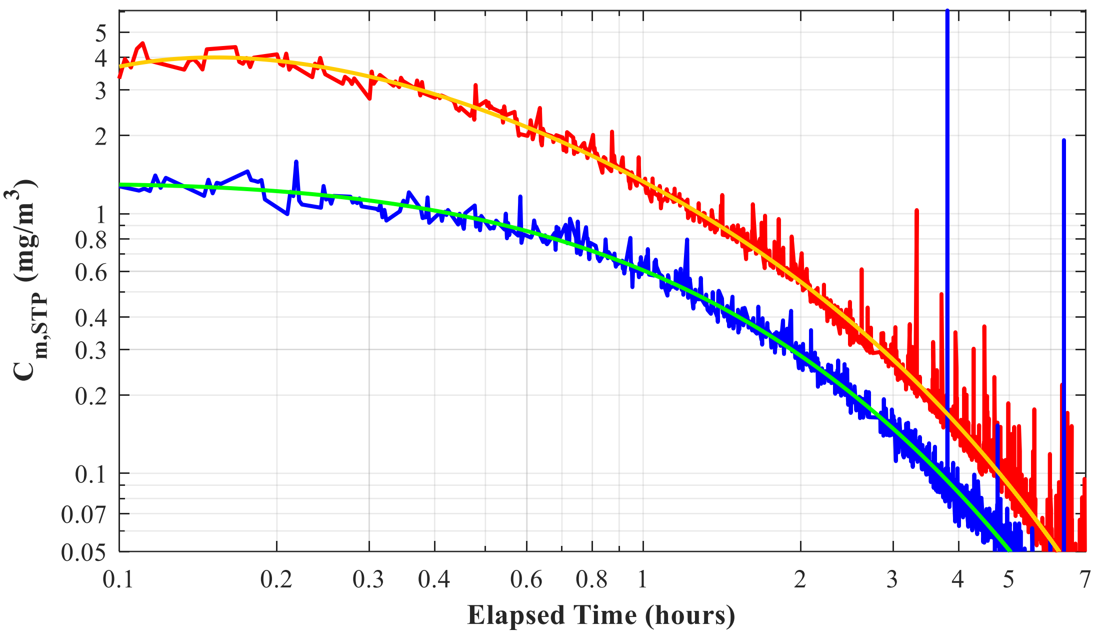

Figure A-16 Raw and curve-fit aerosol mass concentrations for the test on 03/28/2022 with air at constant pressure (ΔP = 715 kPa) and an initial upstream concentration of $C_{m,\,Up,\,STP,\,o}$ = 3.9 mg/m^3 ($C_{m,\,Up,\,o}$ = 31.3 mg/m^3).

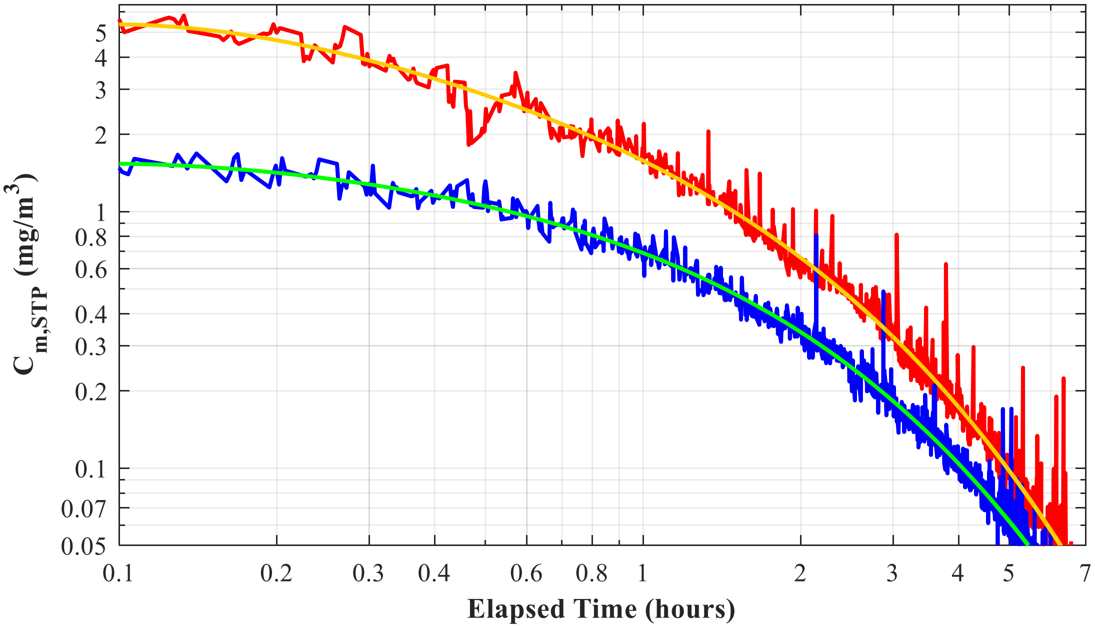

Figure A-17 Raw and curve-fit aerosol mass concentrations for the test on 03/29/2022 with air at constant pressure (ΔP = 716 kPa) and an initial upstream concentration of $C_{m,\,Up,\,STP,\,o}$ = 5.1 mg/m^3 ($C_{m,\,Up,\,o}$ = 40.4 mg/m^3).

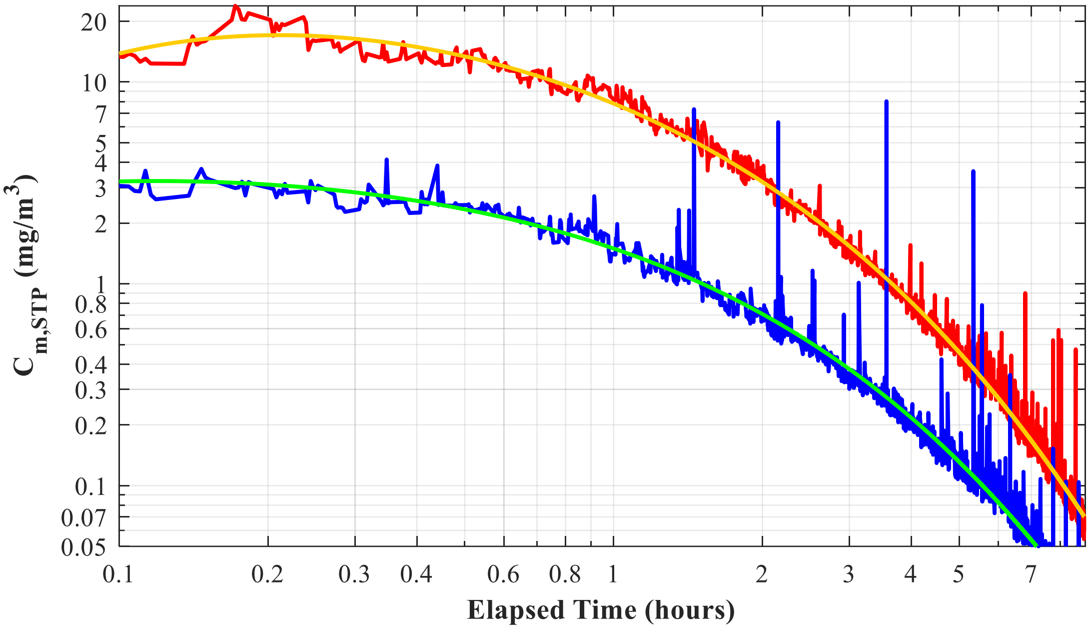

Figure A-18 Raw and curve-fit aerosol mass concentrations for the test on 04/06/2022 with air at constant pressure (ΔP_o = 716 kPa) and an initial upstream concentration of $C_{m,\,Up,\,STP,\,o}$ = 16.1 mg/m^3 ($C_{m,\,Up,\,o}$ = 128.2 mg/m^3).

A.2 Helium Tests

A.2.1 120 kPa Helium

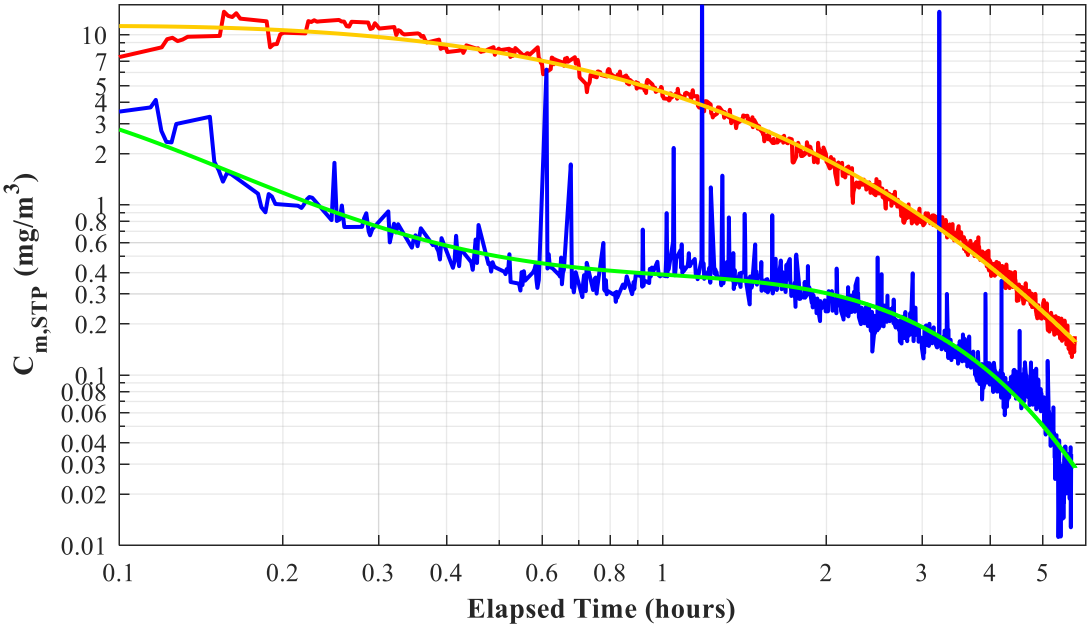

Figure A-19 Raw and curve-fit aerosol mass concentrations for the test on 04/14/2022 with helium at constant pressure (ΔP_o = 119 kPa) and an initial upstream concentration of $C_{m,\,Up,\,STP,\,o}$ = 11.0 mg/m^3 ($C_{m,\,Up,\,o}$ = 22.0 mg/m^3).

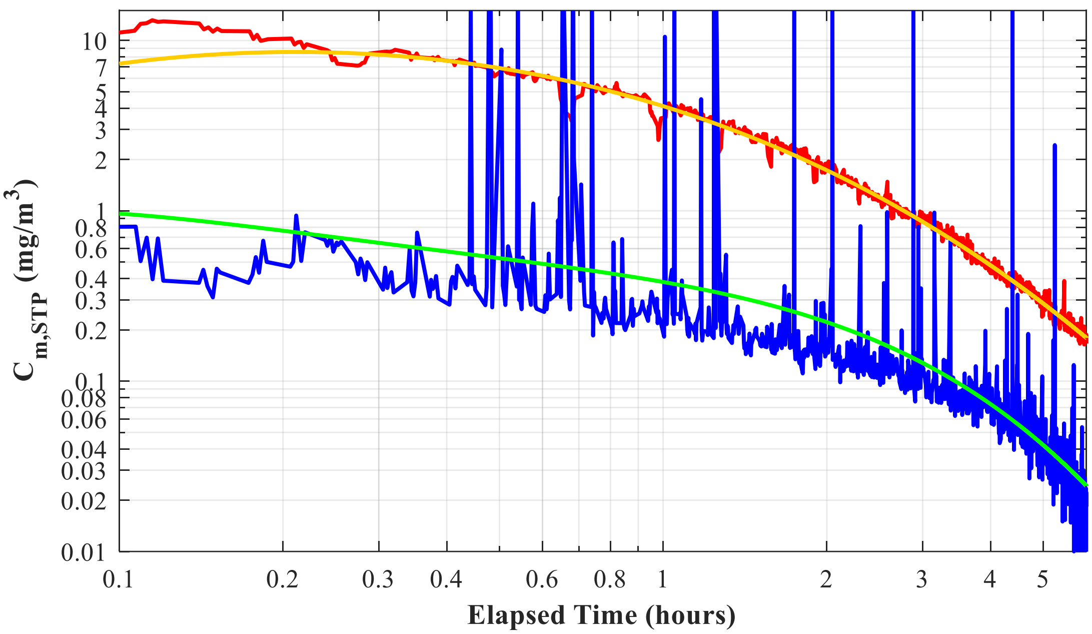

Figure A-20 Raw and curve-fit aerosol mass concentrations for the test on 04/21/2022 with helium at constant pressure (ΔP = 123 kPa) and an initial upstream concentration of $C_{m,\,Up,\,STP,\,o}$ = 8.2 mg/m^3 ($C_{m,\,Up,\,o}$ = 16.5 mg/m^3).

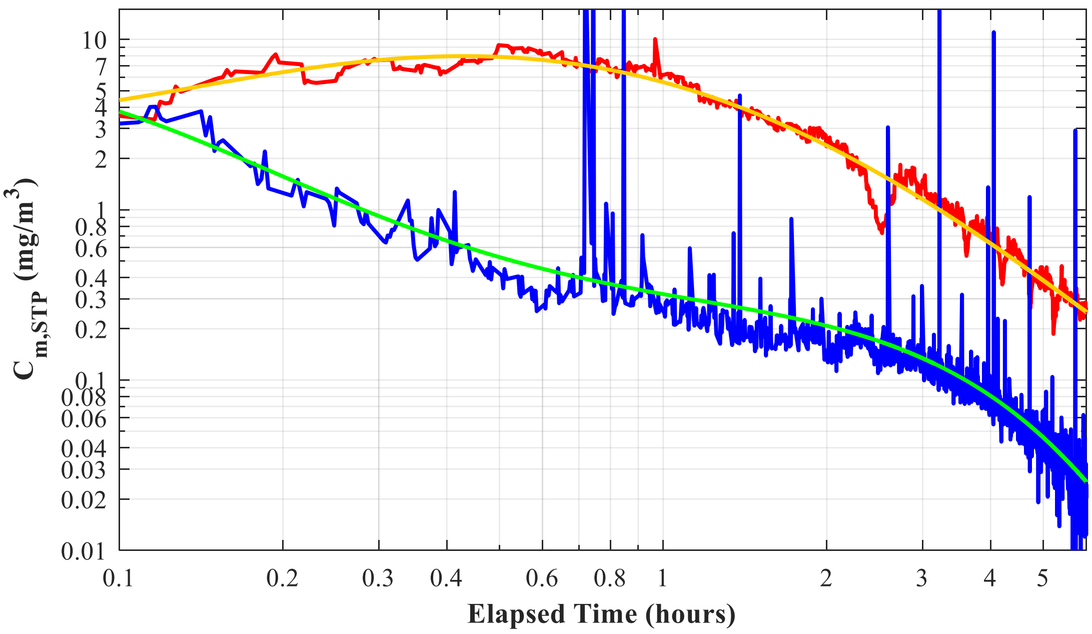

Figure A-21 Raw and curve-fit aerosol mass concentrations for the test on 04/27/2022 with helium at constant pressure (ΔP = 118 kPa) and an initial upstream concentration of $C_{m,\,Up,\,STP,\,o}$ = 5.5 mg/m^3 ($C_{m,\,Up,\,o}$ = 10.9 mg/m^3).

A.2.2 270 kPa Helium

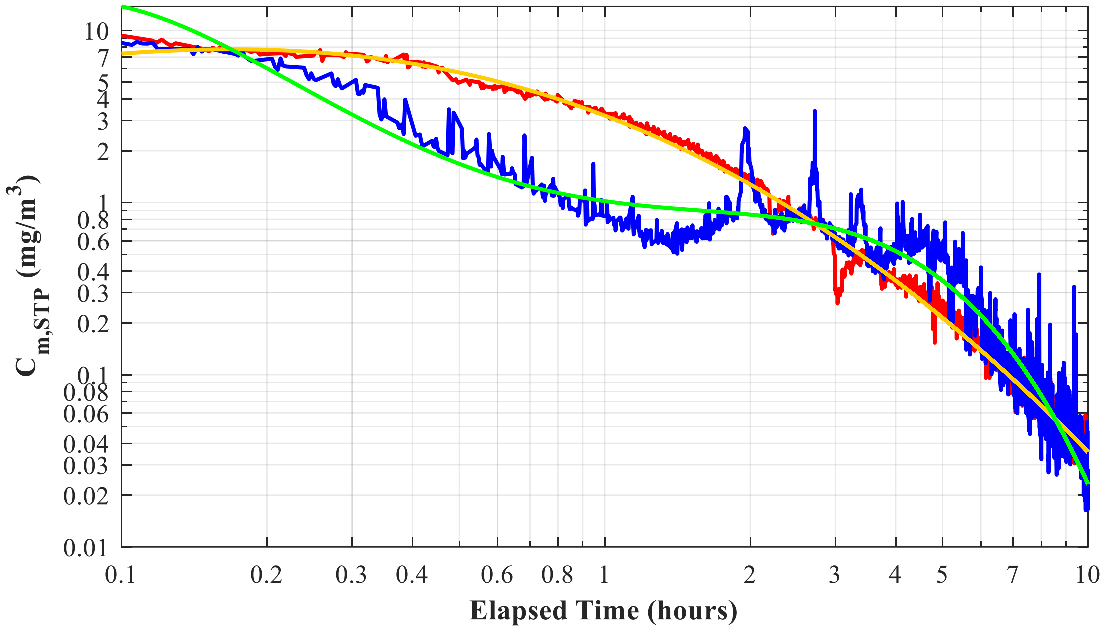

Figure A-22 Raw and curve-fit aerosol mass concentrations for the test on 04/25/2022 with helium at constant pressure (ΔP_o = 249 kPa) and an initial upstream concentration of $C_{m, Up, STP, o}$ = 7.7 mg/m^3 ($C_{m, Up, o}$ = 26.9 mg/m^3).

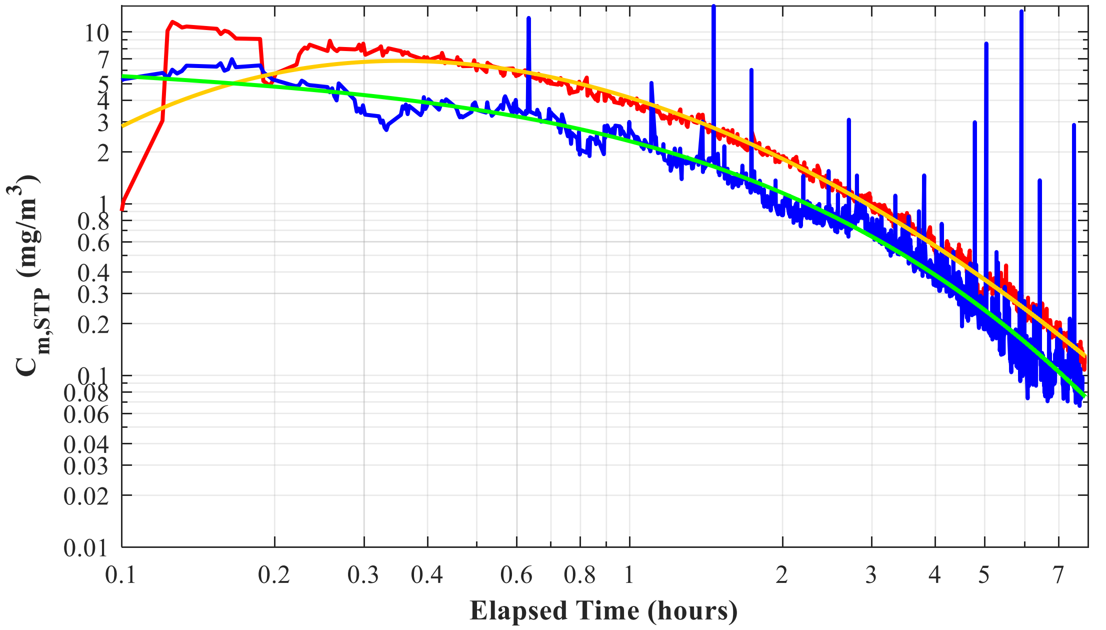

Figure A-23 Raw and curve-fit aerosol mass concentrations for the test on 04/26/2022 with helium at constant pressure (ΔP_o = 266 kPa) and an initial upstream concentration of $C_{m, Up, STP, o}$ = 4.1 mg/m^3 ($C_{m, Up, o}$ = 20.5 mg/m^3).

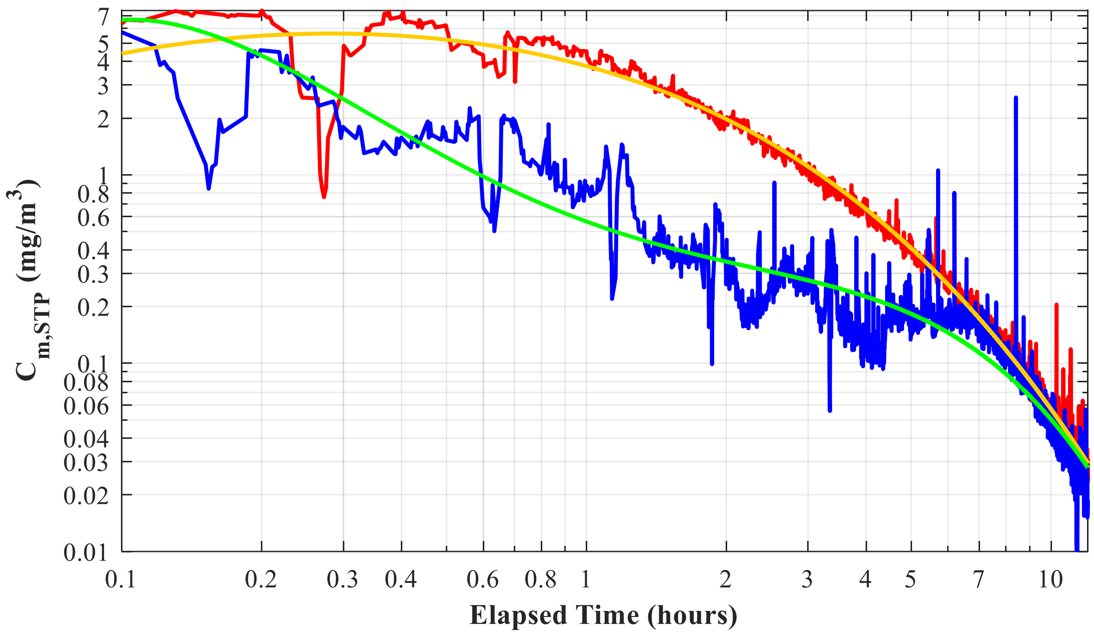

Figure A-24 Raw and curve-fit aerosol mass concentrations for the test on 04/26/2022 PM with helium at constant pressure ($\Delta P_o = 268$ kPa) and an initial upstream concentration of $C_{m,\,Up,\,STP,\,o} = 5.1$ mg/m^3 ($C_{m,\,Up,\,o} = 17.7$ mg/m^3).

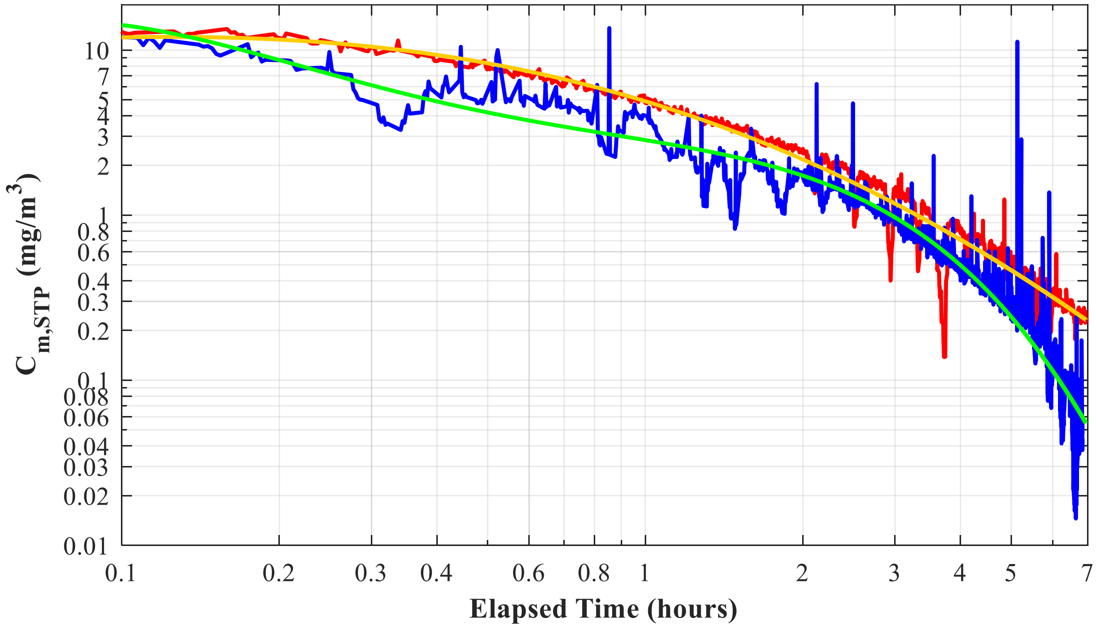

Figure A.5.25 Raw and curve-fit aerosol mass concentrations for the test on 08/01/2022 with helium at constant pressure ($\Delta P_o = 266$ kPa) and an initial upstream concentration of $C_{m,\,Up,\,STP,\,o} = 11.9$ mg/m^3 ($C_{m,\,Up,\,o} = 41.3$ mg/m^3).

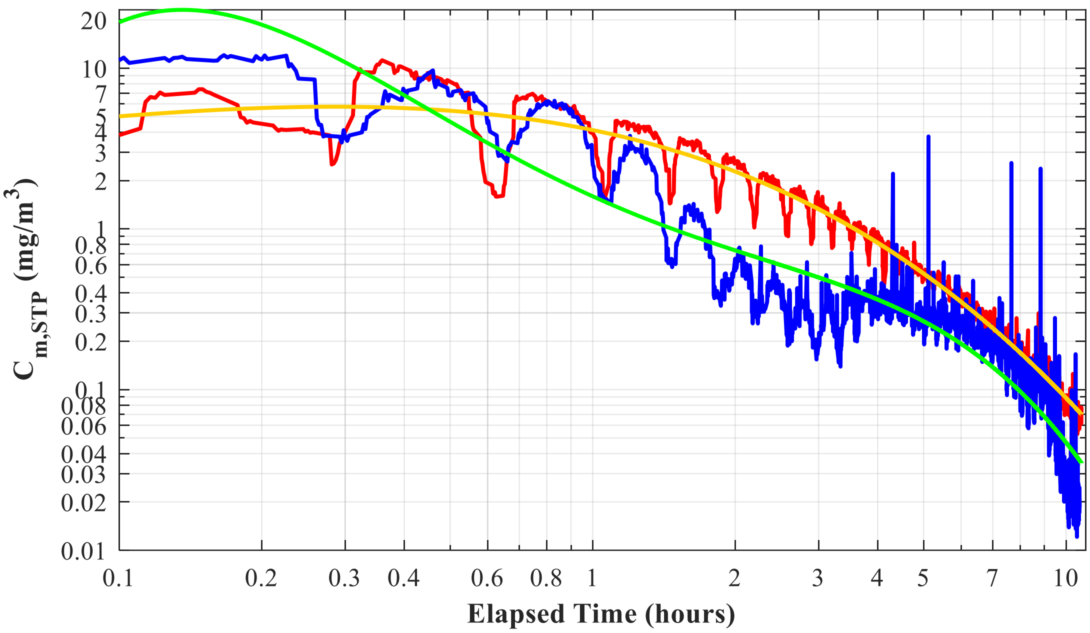

Figure A.5.26 Raw and curve-fit aerosol mass concentrations for the test on 08/02/2022 with helium at constant pressure (ΔP_o = 266 kPa) and an initial upstream concentration of $C_{m, Up, STP, o}$ = 5.4 mg/m^3 ($C_{m, Up, o}$ = 18.8 mg/m^3).

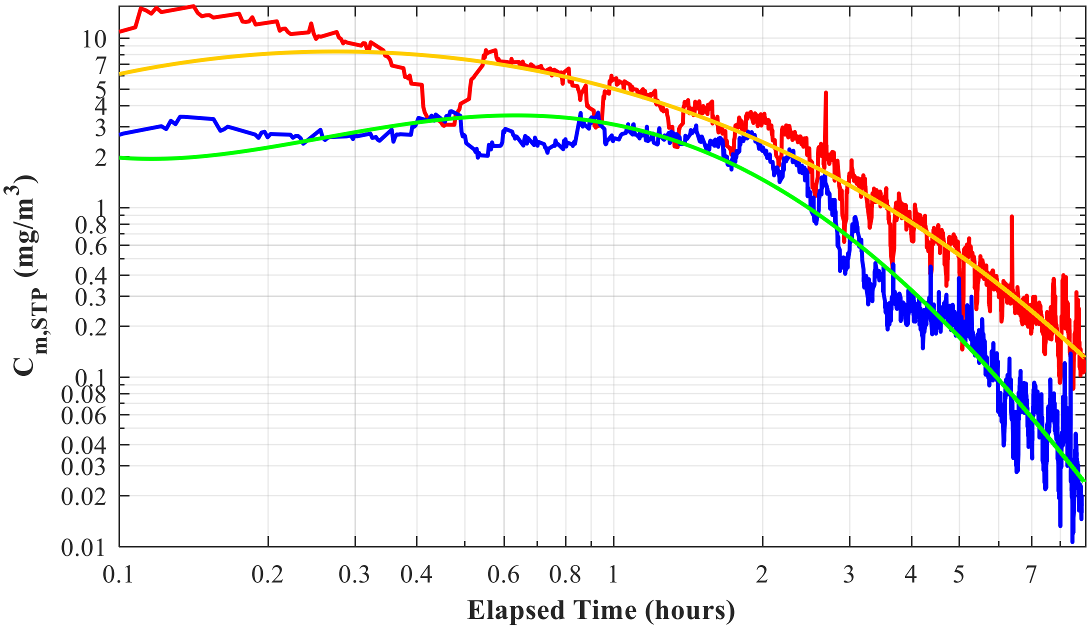

Figure A.5.27 Raw and curve-fit aerosol mass concentrations for the test on 08/03/2022 with helium at constant pressure (ΔP_o = 266 kPa) and an initial upstream concentration of $C_{m, Up, STP, o}$ = 7.4 mg/m^3 ($C_{m, Up, o}$ = 25.5 mg/m^3).

A.2.3 420 kPa Helium

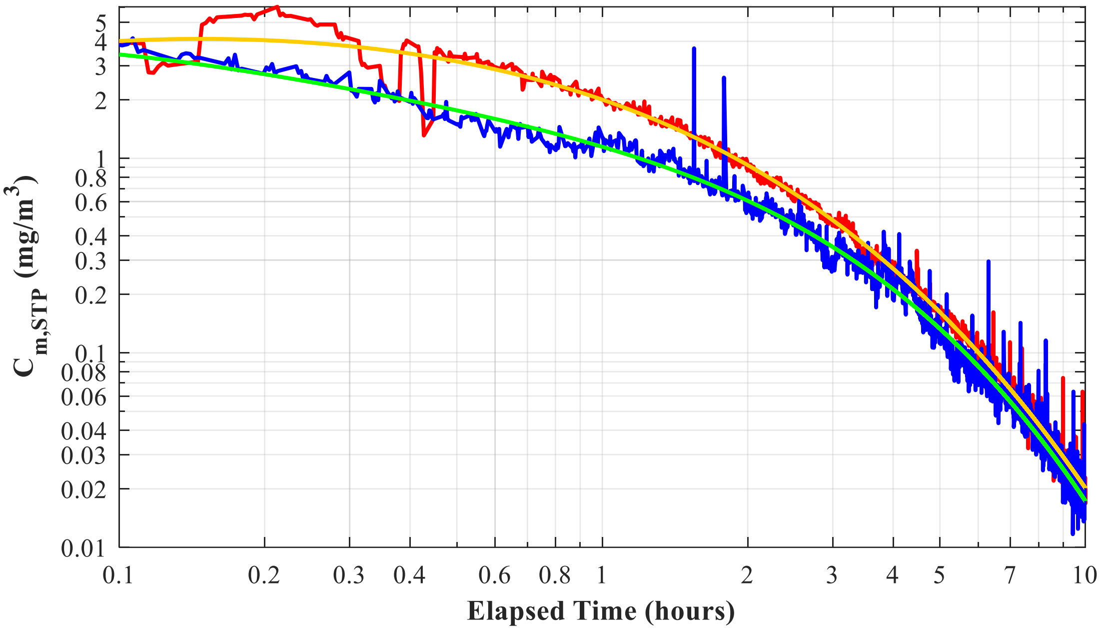

Figure A-28 Raw and curve-fit aerosol mass concentrations for the test on 04/20/2022 with helium at constant pressure (ΔP_o = 424 kPa) and an initial upstream concentration of $C_{m,\,Up,\,STP,\,o}$ = 4.1 mg/m^3 ($C_{m,\,Up,\,o}$ = 20.5 mg/m^3).

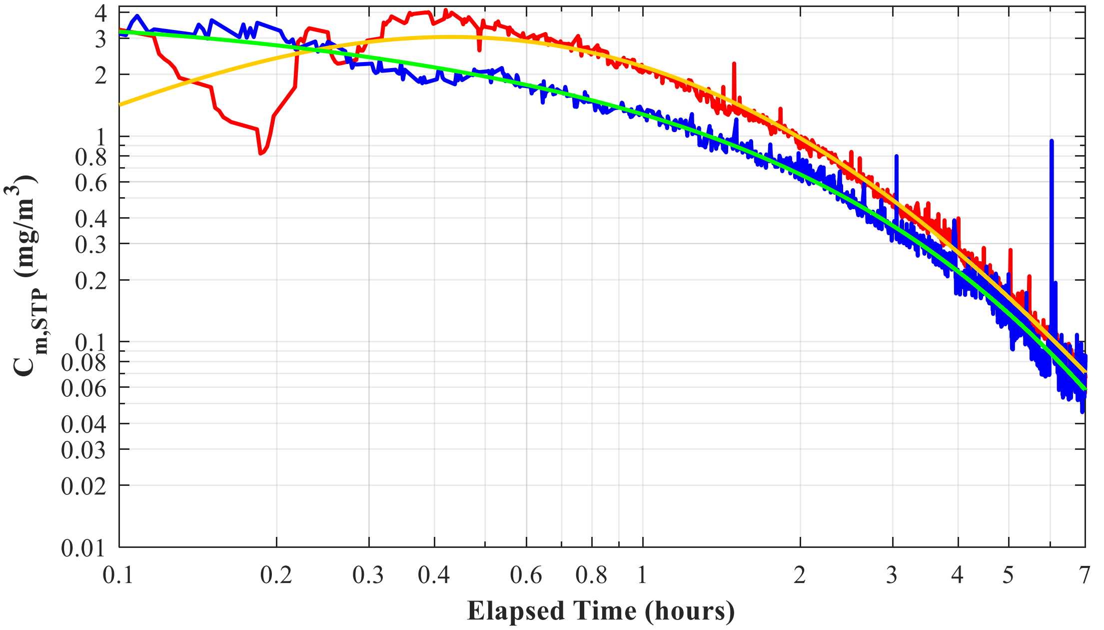

Figure A-29 Raw and curve-fit aerosol mass concentrations for the test on 04/21/2022 with helium at constant pressure (ΔP_o = 417 kPa) and an initial upstream concentration of $C_{m,\,Up,\,STP,\,o}$ = 2.0 mg/m^3 ($C_{m,\,Up,\,o}$ = 9.8 mg/m^3).

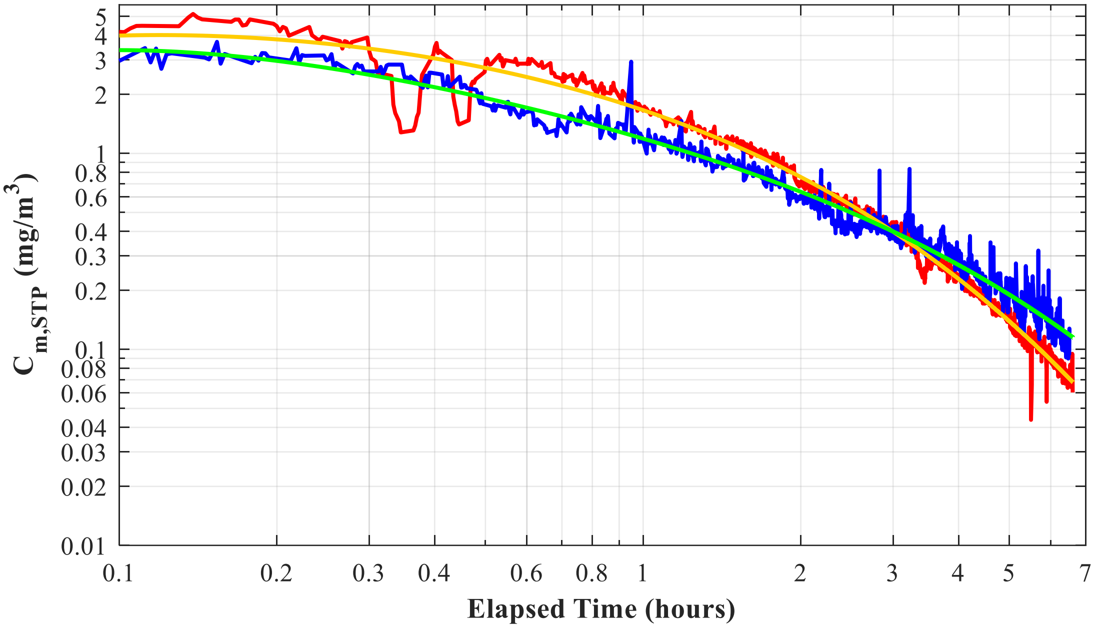

Figure A-30 Raw and curve-fit aerosol mass concentrations for the test on 04/22/2022 with helium at constant pressure (ΔP_o = 424 kPa) and an initial upstream concentration of $C_{m, Up, STP, o}$ = 4.0 mg/m^3 ($C_{m, Up, o}$ = 19.8 mg/m^3).

A.2.4 570 kPa Helium

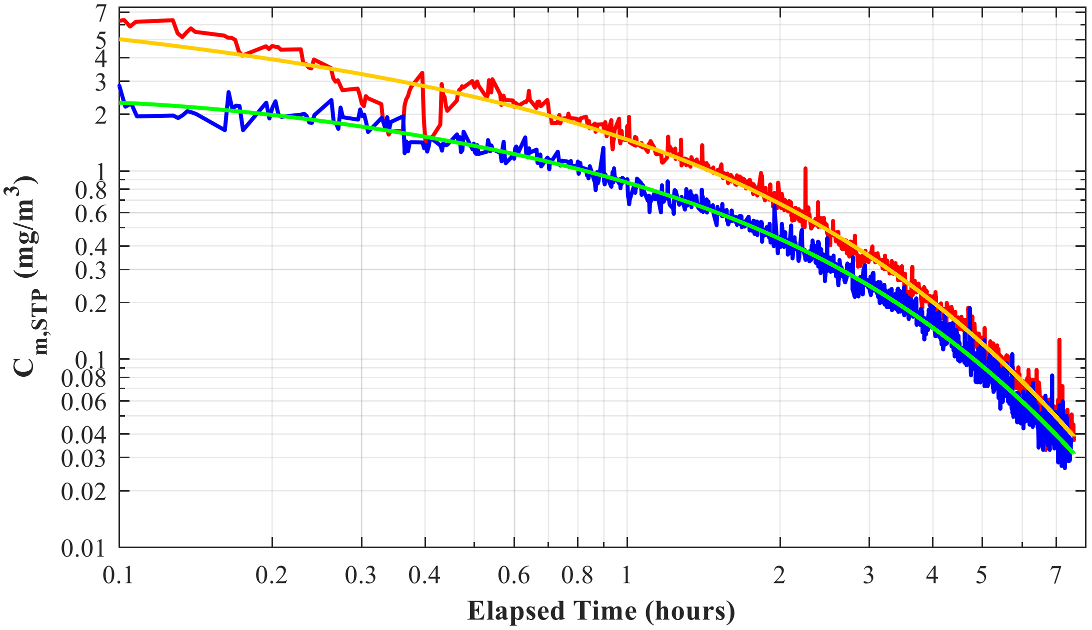

Figure A-31 Raw and curve-fit aerosol mass concentrations for the test on 04/15/2022 with helium at constant pressure (ΔP_o = 566 kPa) and an initial upstream concentration of $C_{m, Up, STP, o}$ = 4.4 mg/m^3 ($C_{m, Up, o}$ = 28.7 mg/m^3).

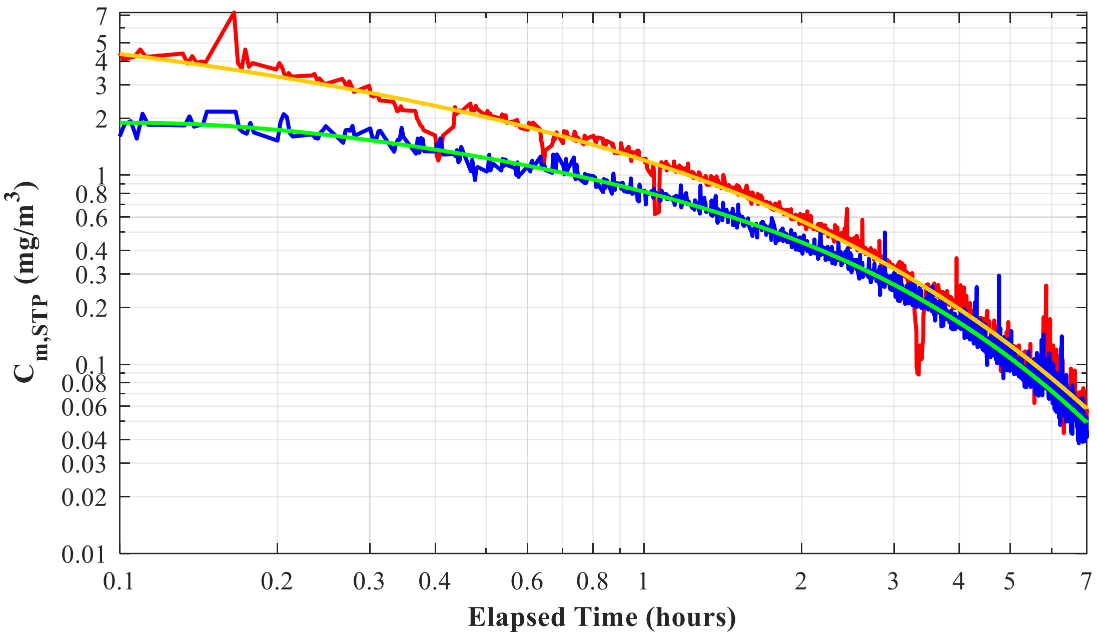

Figure A-32 Raw and curve-fit aerosol mass concentrations for the test on 04/19/2022 with helium at constant pressure (ΔP_o = 568 kPa) and an initial upstream concentration of $C_{m, Up, STP, o}$ = 3.8 mg/m3 ($C_{m, Up, o}$ = 24.6 mg/m3).

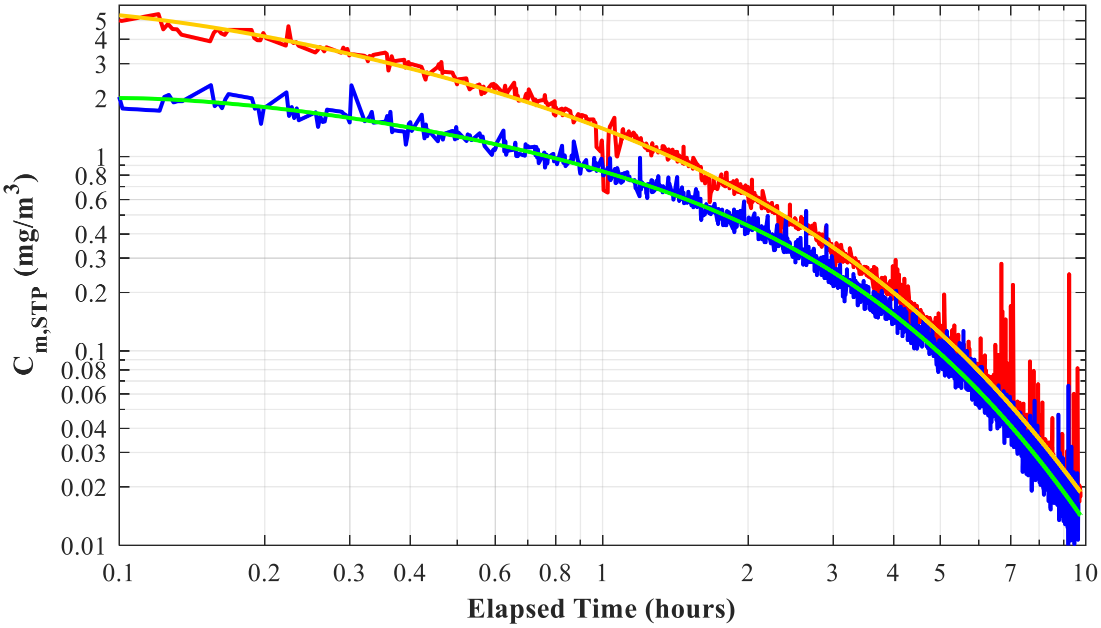

Figure A-33 Raw and curve-fit aerosol mass concentrations for the test on 04/19/2022 PM with helium at constant pressure (ΔP = 566 kPa) and an initial upstream concentration of $C_{m, Up, STP, o}$ = 4.7 mg/m^3 ($C_{m, Up, o}$ = 30.3 mg/m^3).

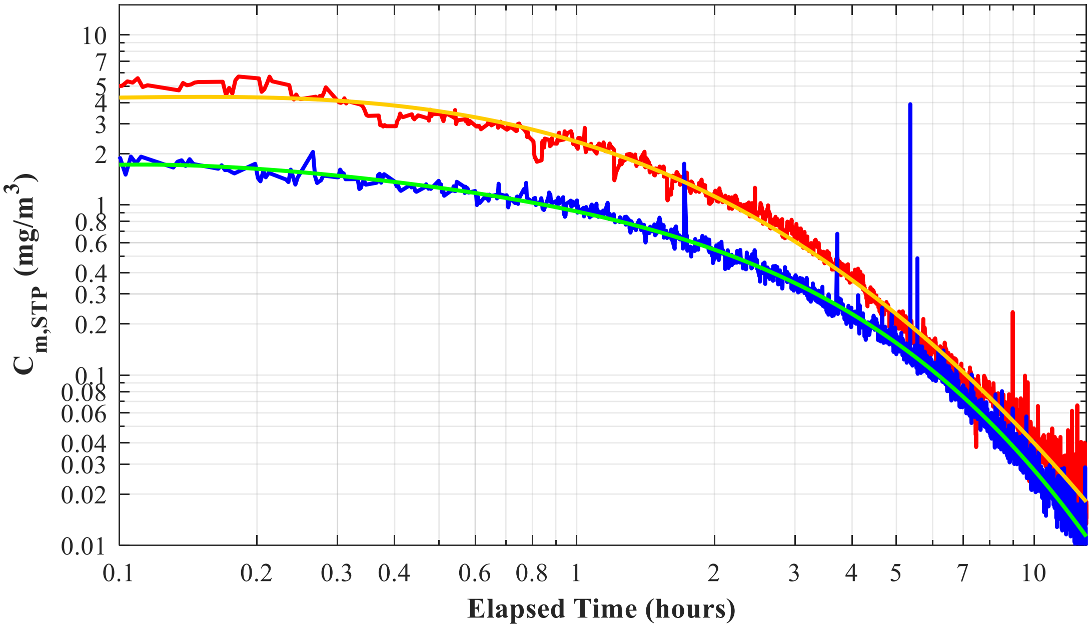

Figure A.5.34 Raw and curve-fit aerosol mass concentrations for the test on 07/19/2022 with helium at constant pressure (ΔP = 566 kPa) and an initial upstream concentration of $C_{m,\ Up,\ STP,\ o}$ = 4.3 mg/m^3 ($C_{m,\ Up,\ o}$ = 27.8 mg/m^3).

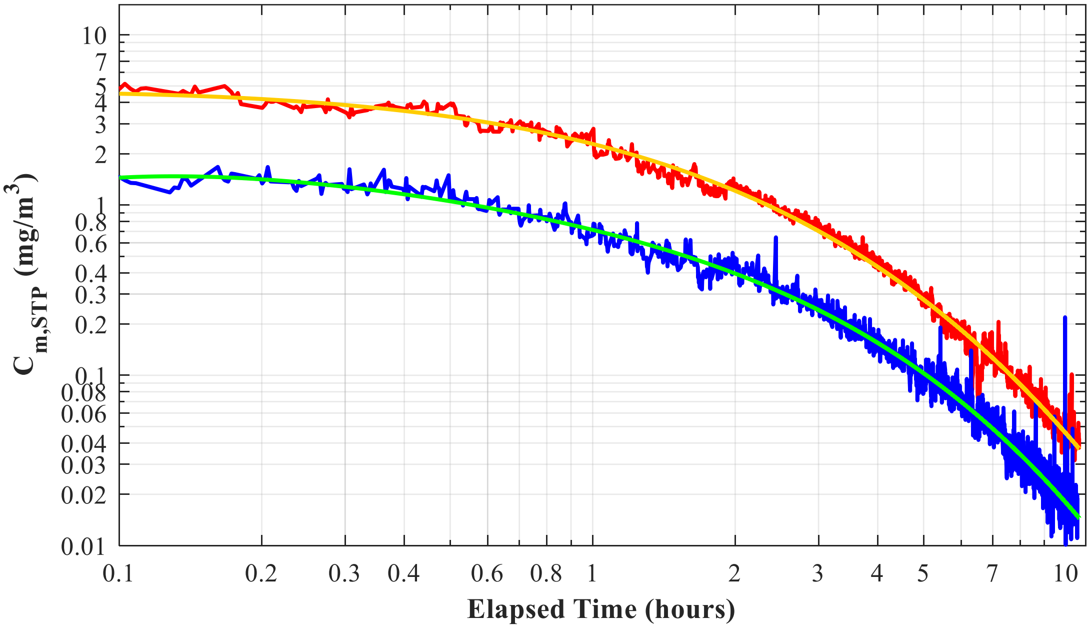

Figure A.5.35 Raw and curve-fit aerosol mass concentrations for the test on 07/20/2022 with helium at constant pressure (ΔP = 565 kPa) and an initial upstream concentration of $C_{m,\ Up,\ STP,\ o}$ = 4.4 mg/m^3 ($C_{m,\ Up,\ o}$ = 28.1 mg/m^3).

A.2.5 720 kPa Helium

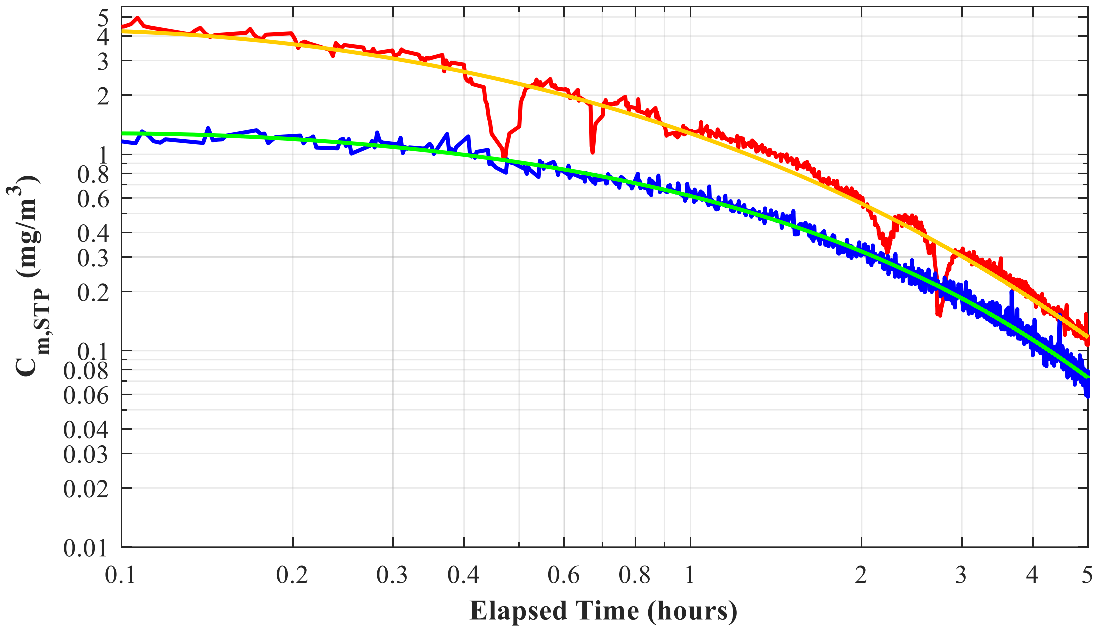

Figure A-36 Raw and curve-fit aerosol mass concentrations for the test on 04/12/2022 with helium at constant pressure (ΔP = 717 kPa) and an initial upstream concentration of $C_{m, Up, STP, o}$ = 3.9 mg/m^3 ($C_{m, Up, o}$ = 31.5 mg/m^3).

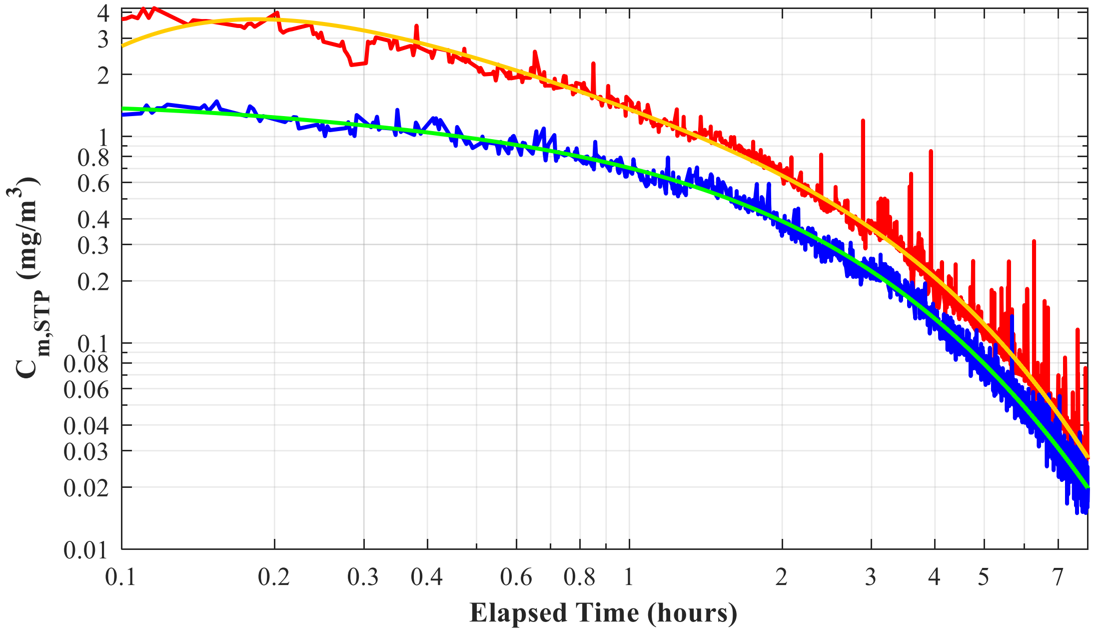

Figure A-37 Raw and curve-fit aerosol mass concentrations for the test on 04/13/2022 with helium at constant pressure (ΔP = 717 kPa) and an initial upstream concentration of $C_{m, Up, STP, o}$ = 3.5 mg/m^3 ($C_{m, Up, o}$ = 27.8 mg/m^3).

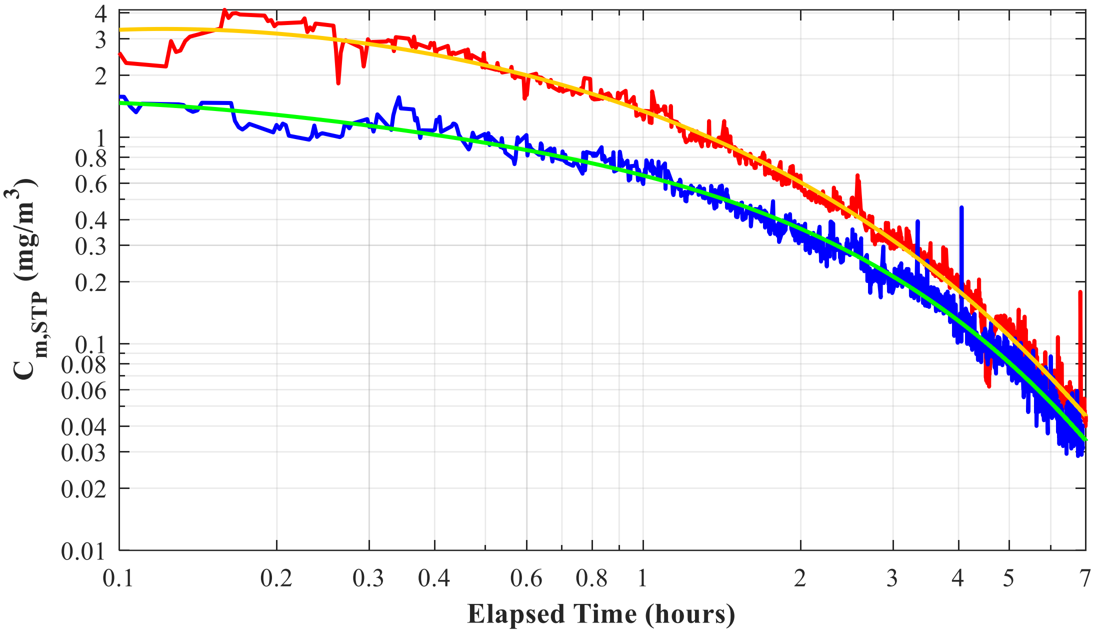

Figure A-38 Raw and curve-fit aerosol mass concentrations for the test on 04/14/2022 with helium at constant pressure (ΔP = 717 kPa) and an initial upstream concentration of $C_{m,\,Up,\,STP,\,o}$ = 3.3 mg/m^3 ($C_{m,\,Up,\,o}$ = 26.4 mg/m^3).

Sandia National Laboratories